



HAL
open science

Spatial-temporal heterogeneity of magma emplacement process and its constraints on localization of associated orebody: A case study in the Shizishan orefield of the Tongling Ore Cluster, east China

Hongsheng Liu, Liangming Liu, Yan Chen, Michel Faure, Xu Xia, Hongzhi Wu, Wei Cao

► To cite this version:

Hongsheng Liu, Liangming Liu, Yan Chen, Michel Faure, Xu Xia, et al.. Spatial-temporal heterogeneity of magma emplacement process and its constraints on localization of associated orebody: A case study in the Shizishan orefield of the Tongling Ore Cluster, east China. *Ore Geology Reviews*, 2021, Accepted manuscript, pp.104587. 10.1016/j.oregeorev.2021.104587. insu-03439459v1

HAL Id: insu-03439459

<https://insu.hal.science/insu-03439459v1>

Submitted on 22 Nov 2021 (v1), last revised 17 Dec 2021 (v2)

HAL is a multi-disciplinary open access archive for the deposit and dissemination of scientific research documents, whether they are published or not. The documents may come from teaching and research institutions in France or abroad, or from public or private research centers.

L'archive ouverte pluridisciplinaire **HAL**, est destinée au dépôt et à la diffusion de documents scientifiques de niveau recherche, publiés ou non, émanant des établissements d'enseignement et de recherche français ou étrangers, des laboratoires publics ou privés.



Distributed under a Creative Commons Attribution 4.0 International License

Journal Pre-proofs

Spatial-temporal heterogeneity of magma emplacement process and its constraints on localization of associated orebody: A case study in the Shizishan orefield of the Tongling Ore Cluster, east China

Hongsheng Liu, Liangming Liu, Yan Chen, Michel Faure, Xu Xia, Hongzhi Wu, Wei Cao

PII: S0169-1368(21)00613-2
DOI: <https://doi.org/10.1016/j.oregeorev.2021.104587>
Reference: OREGEO 104587

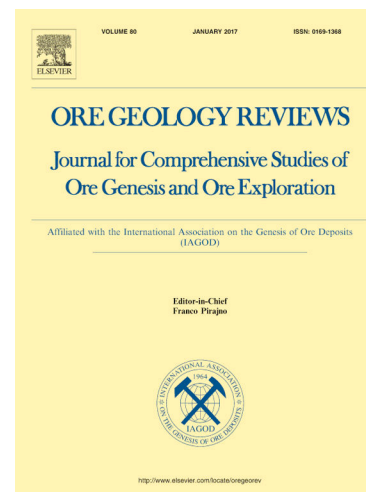
To appear in: *Ore Geology Reviews*

Received Date: 6 September 2020
Revised Date: 12 November 2021
Accepted Date: 14 November 2021

Please cite this article as: H. Liu, L. Liu, Y. Chen, M. Faure, X. Xia, H. Wu, W. Cao, Spatial-temporal heterogeneity of magma emplacement process and its constraints on localization of associated orebody: A case study in the Shizishan orefield of the Tongling Ore Cluster, east China, *Ore Geology Reviews* (2021), doi: <https://doi.org/10.1016/j.oregeorev.2021.104587>

This is a PDF file of an article that has undergone enhancements after acceptance, such as the addition of a cover page and metadata, and formatting for readability, but it is not yet the definitive version of record. This version will undergo additional copyediting, typesetting and review before it is published in its final form, but we are providing this version to give early visibility of the article. Please note that, during the production process, errors may be discovered which could affect the content, and all legal disclaimers that apply to the journal pertain.

© 2021 Published by Elsevier B.V.



Spatial-temporal heterogeneity of magma emplacement process and its constraints on localization of associated orebody: A case study in the Shizishan orefield of the Tongling Ore Cluster, east China

Hongsheng Liu^{a,b}, Liangming Liu^{a,b*}, Yan Chen^c, Michel Faure^c, Xu Xia^d, Hongzhi Wu^{a,b}, Wei Cao^{a,b}

^a School of Geosciences and Info-Physics, Central South University, Changsha, 410083, China.

^b Computational Geosciences Research Centre, Central South University, Changsha, 410083, China.

^c Univ. Orléans, CNRS, BRGM, ISTO, UMR 7327, F-45071, Orléans, France.

^d Tongling Nonferrous Metals Group Holdings Company, Tongling, Anhui, China.

***Corresponding author address:** No. 932 South Lushan Road, Changsha, Hunan Province, 410083 P.R. China

Email address: lmliu@csu.edu.cn (Liangming Liu)

Abstract

We present a study on the Dongguashan quartz diorite stock which is the largest Early Cretaceous intrusion associated with skarn-porphyry polymetallic ore deposit in the Tongling Ore Cluster, Middle-Lower Yangtze Metallogenic Belt in East China. The Dongguashan quartz diorite show massive texture without obvious foliation, and intrusive contact was locally observed inside of the stock. The anisotropy of magnetic susceptibility (AMS) results of the stock show two distinct groups. The Group I (G-I) is dominated by NE-SW-striking magnetic foliation with variably oriented magnetic lineation. The Group II (G-II) that intruded into G-I is characterized by steep NW-SE-striking magnetic foliation and lineation, which are parallel to the vein-like orebody developed in the stock. The 3D geometrical modelling of the stock displays a triangular shape in plan-view with an eastward bulge and irregular stock boundary in the eastern side and the contact surface is steeper in the west than that in the east, denoting that the stock was constructed with an eastward magma accretion trend. Furthermore, the Dongguashan quartz diorite has a wide range of composition and geochronological data, suggesting a multiple magma pulses emplacement model. Accordingly, we propose that the Dongguashan stock was constructed by at least two stages magma pulses. The earlier stage magma pulses intruded along the NE-SW-striking pre-emplacement structures in the country rock and partly intruded into the lithological and mechanical discontinuous interfaces which yielded the stratabound skarn orebody. The eastward magma accretion produced a highly deformed and longer heated country rock on the eastern side of the stock, favoring the orebody development along the eastern stock-country rock contact interface. The late-stage magma pulse and the parallelism among the trend of magnetic foliation of G-II, extensional

structure and vein-like orebody suggest that the vein-type orebodies may controlled by both magma emplacement and regional tectonics.

Keywords: Dongguashan quartz diorite stock; Emplacement mechanism; AMS; Skarn-porphyry deposit; Tongling Ore Cluster

1 **1. Introduction**

2 Study of orebody localization is a key topic for the comprehensive
3 understanding of epithermal metallogenic systems and is indispensable for more
4 efficient exploration of hidden deposits. Nevertheless, orebody localization is a
5 complex geological process that has been contested for decades due to the non-linear
6 relationship among ore-controlling factors and the development of orebodies
7 (Reynolds, 1958; Candela, 1992; Heinrich et al., 1996; Zhao et al., 2010; Liu et al.,
8 2011; Sun and Liu, 2014). Previous geochemical and geochronological studies have
9 revealed that magma intrusions, which determine the type and period of ore-forming
10 process, were the essential ore-controlling factor (e.g., Eugster, 1985; Candela, 1992;
11 Hedenquist and Lowenstern, 1994; Thompson et al., 1999; Hua et al., 2005; Mao et
12 al., 2008, 2011; Sillitoe, 2010; Chen et al., 2012). However, the orebody localization
13 is strongly controlled by the physical and geological conditions of the magma
14 emplacement process, for example, magma ascent rate, emplacement depth, accretion
15 pattern, temperature-pressure and strain field around the intrusion (e.g., Chesley et al.,
16 1993; Duuring and Hagemann, 2001; Candela et al., 2005; Vigneresse, 2006, 2007;
17 Eldursi et al., 2009; Holwell et al., 2014; Chen and Nabelek, 2017; Schöpa et al.,
18 2017). Moreover, the geometries of pluton and pluton-country rock contact were also
19 considered as important ore-controlling factors (Romeo et al., 2008; Liu et al., 2011,
20 2014; Chicharro et al., 2015; Cao et al., 2020). Hence, the reconstruction of the
21 magma emplacement process and 3D geometry of plutons is crucial for understanding
22 the mechanism of orebody localization.

23 Anisotropy of magnetic susceptibility (AMS) is a successful method to reveal
24 the magma emplacement process, as the pattern of magnetic fabric can reflect the
25 magma flow direction, magma accretion and regional tectonic setting (e.g., Hrouda,
26 1982; Ernst and Baragar, 1992; Rochette et al., 1992; Bouchez, 1997). In addition,
27 with the development of computational modelling methods, the pluton geometry can
28 be well defined by geophysical and borehole data (e.g., Améglio et al., 1997; Romeo
29 et al., 2008; Liu et al., 2012; Lü et al., 2013; Sun and Liu, 2014; Wei et al., 2014).
30 However, the application of AMS is usually impeded by limited surface exposures of
31 the pluton, and the pluton geometry remains unclear due to the multi-use
32 interpretation of geophysical data.

33 The Shizishan orefield is a representative skarn-porphyry ore deposit that is
34 related to the Late Mesozoic intrusion and located at the center of the Tongling Ore
35 Cluster, Middle-Lower Yangtze Metallogenic Belt, East China (rectangle inset in Figs.
36 1 and 2). In this study, we chose the Dongguashan quartz diorite stock as our research
37 target (Fig. 3) as it is the largest ore-forming intrusion in the Shizishan orefield.
38 Furthermore, the Dongguashan quartz diorite stock has been previously well studied
39 in geochemistry, geochronology and geophysics (Xu et al., 2005, 2008, 2010; Deng et
40 al., 2006; Xie et al., 2012; Guo et al., 2013; Wang et al., 2015; Cao et al., 2016; Liu et
41 al., 2018). However, the localization mechanism of these randomly developed
42 skarn-porphyry orebodies around the stock is still ambiguous. The Dongguashan
43 quartz diorite stock has been highly explored, and mining shafts and platforms have
44 been constructed from the surface to -850 m in the depth, so that the AMS sampling

45 can cover the deep part of the Dongguashan quartz diorite stock. Moreover, with help
46 of the intensive drilling projects in this area, the geometry of the stock and its related
47 orebodies can be also reliably constructed. Therefore, through the field observation,
48 AMS measurement, 3D geometry modeling and geochemical analysis of the stock, we
49 acquired the distribution of magnetic fabric inside the stock, 3D geometry of the stock,
50 as well as the variation of geochemical composition. Accordingly, we deciphered the
51 development of the Dongguashan quartz diorite stock and the constraints on
52 associated orebodies. Our study can help to guide the deep prospecting in the
53 Middle-Lower Yangtze Metallogenic Belt and has implications that bear on other
54 large-scaled intrusions.

55 **2. Geological background**

56 *2.1. Regional geological setting*

57 The Middle-Lower Yangtze Metallogenic Belt (Fig. 1a and b) is one of the most
58 important Cu-Au-polymetallic belts in China, and in the world as well. It is a typical
59 skarn-porphyry deposit belt related to Late Mesozoic intrusions developed in an
60 intracontinental setting (Chang et al., 1991; Pan and Dong, 1999; Mao et al., 2011;
61 Zhou et al., 2015). Hundreds of studies on these intrusions and their influences on the
62 related skarn ore deposit had been done in the Middle-Lower Yangtze Metallogenic
63 Belt, for examples, the geochronological, geochemical and petrological characteristics
64 of the intrusions (e.g., Wang et al., 2004; Xie et al., 2009, 2017; Zhang et al., 2010;
65 Yang et al., 2011; Yang and Lee, 2011; Wu et al., 2013), the origin of the
66 hydrothermal fluid (e.g., Zhou et al., 2000, 2007; Lai et al., 2007; Gu et al., 2011; Cao

67 et al., 2012; Li et al., 2019; Liu et al., 2019), and the geodynamic setting and related
68 implications for metallogeny (e.g., Deng et al., 2011; Mao et al., 2011; Shi et al., 2013;
69 Lü et al., 2015).

70 The Tongling Ore Cluster (TOC; rectangle inset in Figs. 1b and 2) is located in
71 the center of the Middle-Lower Yangtze Metallogenic Belt, where Early Cretaceous
72 dioritic intrusions are widely developed and often associated with skarn-porphyry
73 Cu-Au ore deposits (Fig. 1b). The TOC consists of the Tongguanshan, Shizishan,
74 Xinqiao, Fenghuangshan and Shatanjiao orefields (Xie et al., 2017; Fig. 2). The
75 stratigraphy of the TOC includes Lower Silurian to Upper Devonian siltstone,
76 quartz-sandstone and silty shale, Middle Carboniferous to Early Triassic limestone,
77 siliceous shale, calcareous shale and dolomite, and Late Mesozoic to Tertiary
78 dolomitic limestone, clay shale, volcanic rocks, and continental clastic rocks (Zhai et
79 al., 1992; Xu and Zhou, 2001). Structurally, the TOC is characterized by
80 NE-SW-striking upright folds and high-angle NW- or SE- directed thrusts, and
81 subordinate NNE-, NNW- and NW-striking brittle faults (Fig. 2; Chang et al., 1991;
82 Tang et al., 1998). This structural pattern is considered to be an inherited structure that
83 represents repeated NW-SE directed compressional regional tectonic setting. In
84 particular, this includes the Middle Triassic intracontinental subduction of South
85 China Block under the North China Craton (Lin et al., 1985; Zhao and Coe, 1987;
86 Mao et al., 2011), and the southwestward subduction of the Izanagi plate under the
87 east Eurasian plate since the Late Jurassic (Sun et al., 2007; Li et al., 2011). Moreover,
88 the NE-SW-striking Early Cretaceous Luzong and Ningwu volcanic basins and

89 widespread Early Cretaceous intrusions and volcanism in the TOC suggest a
90 predominantly extensional regional tectonic setting in the Early Cretaceous period
91 (Deng et al., 2011).

92 **2.2. The Dongguashan stock**

93 Several Early Cretaceous intrusions are exposed in the Shizishan orefield (Fig.
94 3), including the Dongguashan quartz diorite (138.4 ± 1.7 Ma; Wu et al., 2013), the
95 Baimangshan pyroxene monzodiorite (139.9 ± 1.9 Ma; Guo et al., 2013), the
96 Jiguanshi pyroxene-quartz monzodiorite (139.8 ± 0.8 Ma; Wu et al., 2008), and the
97 Hucun granodiorite (140 ± 2.6 Ma; Xu et al., 2008). The Dongguashan quartz diorite
98 belongs to metaluminous and high-K, calc-alkaline-series granite (delineated by white
99 dash line in Fig. 3; Wu et al., 2010; Liu et al., 2018). Previous geobarometric studies
100 on the contemporary Cretaceous intrusions in this area and geophysical investigations
101 indicate that the Dongguashan quartz diorite stock was emplaced at the brittle crust
102 depth (ca. 4-6 km; Du et al., 2004). The Dongguashan quartz diorite stock intruded in
103 the hinge and eastern limb of the NE-trending Qingshanjiao anticline, which is
104 considered as the major ore-controlling structure in the Shizishan orefield (Lu et al.,
105 2003; Xu et al., 2005; Lü et al., 2013; Liu et al., 2014). Country rocks exposed on the
106 surface are Middle to Lower Triassic limestone, argillaceous limestone and argillite,
107 which were folded by the Middle to Late Triassic intracontinental orogenic event (Liu
108 et al., 2014).

109 **2.3. Ore deposit**

110 With at least 10 exploited ore deposits and copper and gold reserves of more

111 than 1.5 Mt and 20 t, respectively (Xu et al., 2014), the Shizishan orefield is
112 economically the most important Cu-Au district in the TOC. Especially the proven
113 copper and gold reserves of the Dongguashan ore deposit are 0.98 Mt at 1.01% and 29
114 t at 0.26 g/t, respectively (Liu et al., 2014, 2018). According to previous studies, there
115 are three major ore localization zones around the Dongguashan stock, i.e. the
116 Dongguashan, Datuanshan and Huashupo ores.

117 **3. Field observation and sampling**

118 The Dongguashan quartz diorite stock is not well exposed on the surface (Fig.
119 3), and fresh quartz diorite outcrops were revealed only by the ore exploration. The
120 Dongguashan stock mainly consists of medium to fine grained quartz diorite (Fig. 4a
121 and b) and porphyritic quartz diorite occurs locally along the stock-country rock
122 contact (Fig. 4c). The Dongguashan quartz diorite usually displays a massive texture
123 without macroscopic foliation, but oriented hornblende grains with sub-horizontal and
124 outward dipping plunge are locally observed in the contact zone (Fig. 4b).
125 Metamorphosed country rock xenoliths are observed in the stock margin (Fig. 4d and
126 e), which resemble the “exploding xenoliths” texture observed in the shallow level
127 intrusions (Clark et al., 1998; de Saint-Blanquat et al., 2001). Moreover, the
128 disharmonic folding of limestone strata (Fig. 4f) can be observed, suggesting the
129 existence of decollement sliding in the country rocks.

130 The orebody developed around the Dongguashan quartz diorite stock is
131 characterized by stratiform (Fig. 5a), massive (Fig. 5b), veinlet and vein-like textures
132 (Fig. 5c and d). The major sulfides are chalcopyrite, pyrite, magnetite, pyrrhotite, and

133 the major gangue minerals are calcite and dolomite. Furthermore, our field
134 investigation found widely developed extension related structures. For example, (1)
135 the large-scale fracture zone developed in the stock with occurrence of $120^{\circ}/66^{\circ}\text{SW}$
136 (Fig. 5b), (2) the conjugated vein-type chalcopyrite ore dipping to SW and NE (ca. 0.5
137 to 2 cm in width; Fig. 5c and e), and (3) widely developed southwest dipping calcite
138 veins in the stock and its country rocks (Fig. 5d and f).

139 According to the architecture and layout of the mine shaft and platforms in the
140 study area, we have chosen seven mine platforms for AMS sampling, i.e. -390 m,
141 -460 m, -580 m, -670 m, -730 m, -790 m and -850 m. A total of 41 AMS sampling
142 sites have been collected at different depths from -390m to -850m, which are evenly
143 distributed along the accessible mining channels with an interval of ca. 100 m. Due to
144 the limited resolution of the GPS signal in the mining channels and short distances
145 between different sites, the locations of AMS sampling are presented on the plan-view
146 of the stock. The AMS samples were collected with a portable gasoline drill and
147 oriented using a magnetic compass. The collected core samples were cut into standard
148 cylindrical specimens, i.e. 2.2 cm in height and 2.5 cm in diameter, for AMS
149 measurements. Detailed sampling information is listed in Table 1.

150 Concurrently, representative massive fresh quartz diorite samples were collected
151 from the -670 m platform, which is the largest section of the Dongguashan stock
152 revealed by current mining projects, for geochemical analysis in order to investigate
153 the horizontal variation of composition inside the stock. The locations of these
154 samples are the same as the AMS sample at this platform.

155 **4. Analytical methods**

156 **4.1. Anisotropy of Magnetic Susceptibility (AMS)**

157 The magnetic susceptibility (K) is defined as the ratio of the induced
 158 magnetization (M) to the applied field (H), while the intensity of magnetization is
 159 usually nonuniform due to the preferred orientation of minerals in the rock (Hrouda,
 160 1982; Tarling and Hrouda, 1993), which is named as the Anisotropy of the Magnetic
 161 Susceptibility (AMS). The AMS is a second-order tensor of the magnetic
 162 susceptibility in a preferred direction, and it can be expressed by a magnetic
 163 susceptibility ellipsoid with three mutually perpendicular susceptibility axes, i.e.
 164 $K_1 \geq K_2 \geq K_3$ (Tarling and Hrouda, 1993; Borradaile and Jackson, 2004). K_1 and K_3
 165 represent the magnetic lineation and pole to the magnetic foliation, respectively.
 166 Moreover, several parameters were calculated with the measured values of K_1 , K_2 and
 167 K_3 by the program Anisoft (version 4.2, AGICO), for example, the mean bulk
 168 magnetic susceptibility ($K_m = 1/3(K_1 + K_2 + K_3)$), the corrected degree of anisotropy
 169 ($P_J = \exp\sqrt{2[(\eta_1 - \eta)^2 + (\eta_2 - \eta)^2 + (\eta_3 - \eta)^2]}$) and the shape parameter
 170 ($T = (2\eta_2 - \eta_1 - \eta_3) / (\eta_1 - \eta_3)$), where $\eta_n = \ln K_n$ and $\eta = (\eta_1 + \eta_2 + \eta_3) / 3$. K_m indicates the mean
 171 bulk magnetic susceptibility of different magnetic carriers, including the
 172 ferromagnetic, paramagnetic and diamagnetic minerals, and the P_J and T values
 173 represent the eccentricity and shape of the magnetic ellipsoid, respectively (Jelínek,
 174 1978, 1981; Hrouda, 1982).

175 The mineralogical investigations, including thermomagnetic measurement,
 176 Isothermal Remanence Magnetization (IRM) and hysteresis properties, were

177 conducted on representative samples to reveal the contribution of different magnetic
178 carriers to the bulk magnetic susceptibility. The thermomagnetic measurements were
179 performed at the Paleomagnetism Laboratory of Nanjing University with the CS3
180 furnace coupled with a KLY-3S Kappabridge, and protective argon gas was used. The
181 samples were heated from 50° to 700° with constant heating and cooling rate of
182 9°/min. The hysteresis loops and IRM measurement were carried out at the Key
183 Laboratory of Paleomagnetism and Tectonic Reconstruction of Ministry of Natural
184 Resources (Beijing). Magnetic hysteresis loops and FORCs can reveal both the grain
185 size and domain state of magnetic minerals and were obtained using a Lakeshore
186 8600 Vibrating Sample Magnetometer (VSM). For the magnetic hysteresis loop
187 experiments, the powdered samples were subjected to a cycled field of ± 600 mT. A
188 slope correction was applied to remove the impact of paramagnetic contributions.

189 ***4.2. Whole-rock major and trace element analyses***

190 Whole-rock major and trace element analyses were conducted at the ALS
191 Chemex Co., Ltd (Guangzhou, China). The major element concentration was
192 determined by an X-ray fluorescence (XRF) spectrometer with an analytical precision
193 better than $\pm 0.01\%$. Trace elements were measured using PerkinElmer ICP-MS with
194 an analytical precision better than $\pm 5\%$ for most elements. Detailed analytical
195 methods and procedures can be found in Liang et al. (2000).

196 ***4.3 3D geometry modelling***

197 The 3D geometry of the Dongguashan quartz diorite stock and its related ore
198 deposit was mainly defined by the borehole data from the Tongling Nonferrous

199 Metals Group Holdings Company. All these data were integrated in the Micromine
200 and GOCAD platforms, and the boundary of the geological body at shallow levels
201 (<-850 m) without borehole data was mainly deduced by using the Micromine
202 platform with Kriging interpolation and smoothed at the COCAD platform. Detailed
203 approaching process is reference to Liu et al. (2012).

204 **5. Results**

205 *5.1. Petrographic texture investigation*

206 A total of twenty-four core specimens were selected from forty-one AMS
207 sampling sites to prepare the oriented thin sections for petrographic texture
208 investigation (Fig. 6a). The Dongguashan quartz diorite mainly consists of plagioclase,
209 K-feldspar, quartz, biotite, hornblende, and is associated with sphene, magnetite,
210 pyrite, apatite and zircon (Fig. 6b-6e). Some of the Dongguashan quartz diorites
211 display a porphyritic texture, characterized by relatively larger feldspar crystals (Fig.
212 6b-6e). The minerals show a euhedral to sub-euhedral habitus, and no textures related
213 to sub-solidus high temperature deformation have been observed. Sericitization is
214 usually developed along the cleavage of the minerals (Fig. 6b). Magnetite and pyrite
215 are widely distributed in all the samples and are present in interstitial clots and aligned
216 parallel to the long axis of the minerals (Fig. 6f) or in interstitial crystals (Fig. 6g).

217 *5.2. AMS of the Dongguashan stock*

218 *5.2.1 Rock magnetic minerals*

219 Six representative thermomagnetic measurements were performed. The heating
220 curves show a gradual decreasing trend indicating the existence of paramagnetic

221 minerals (Fig. 7a-7f). A moderate to slight drop at 325 °C for the samples collected
222 from the depths shallower than -670 m suggests the presence of pyrrhotite (Fig.
223 7a-7d), and a rapid drop at 580 °C for all the samples is most likely due to the
224 existence of magnetite (Fig. 7a-7f). An obvious increase of magnetic susceptibility
225 during cooling implies that mineralogical phase transformation occurred during the
226 thermal experiment, for instance, pyrrhotite and pyrite transformed into magnetite at ~
227 500 °C (Dunlop and Özdemir, 1997). The shapes of the hysteresis loops of these
228 samples are similar to that of ferromagnetic minerals (Fig. 7h-7j) with low values of
229 magnetic coercivity (Fig. 7k-7m). Moreover, the isothermal remanence measurements
230 show similar rapid increasing and saturation trend at ca. 300 mT (Fig. 7k-7m).
231 Accordingly, the magnetic minerals in the Dongguashan quartz diorite are composed
232 of paramagnetic minerals, e.g., biotite and feldspar, and low-coercivity ferromagnetic
233 minerals, e.g., magnetite and pyrrhotite. The thin section observations show a
234 relatively high volume-ratio of magnetite (Fig. 6e-6f), suggesting that the magnetite
235 may be the major magnetic susceptibility carriers in the Dongguashan quartz diorite.

236 5.2.2. *Magnetic parameter data*

237 The magnetic parameters of quartz diorite in the Dongguashan stock, for
238 instance, K_m , P_J and T , are provided in Table 1, and K_m vs. P_J and T vs. P_J diagrams
239 are presented in figure 8. More than 90% sites show high bulk magnetic susceptibility,
240 i.e. $K_m > 10^{-3}$ SI (Fig. 8a), confirming that these samples are dominated by the
241 ferromagnetic minerals. Moreover, no linear correlation has been observed between
242 the bulk magnetic susceptibility and corrected degree of anisotropy, denoting that the

243 magnetic fabric is mainly defined by the rock composition (Borradaile, 1988). Over
244 seventy percent of sites have corrected degree of anisotropy values lower than 1.15
245 (Table 1 and Fig. 8a), indicating that the magnetic fabric is mainly primary (Hrouda,
246 1982; Rochette et al., 1992). The sites with high P_J value are close to the stock
247 boundary, which may be due to the intense interaction of the magma intrusion with
248 the country rocks (Table 1 and Fig. 8). The majority of shape parameter values are
249 positive (Table 1 and Fig. 8b), suggesting the prevalence of oblate ellipsoids, except
250 for samples collected from the south part of the stock, which are dominated by
251 negative values (Table 1 and Fig. 9), and thus, prolate magnetic ellipsoids are
252 suggested.

253 *5.2.3 Magnetic fabrics*

254 Detailed site-mean magnetic fabrics and their positions with respect to the
255 restored stock boundary at depth are presented in Fig. 9. Most of these sites show well
256 developed magnetic foliations with inclinations from highly inclined dipping (40°) to
257 vertical (89°), except for sites DTS14, HSP25 and DGS34 with gentle inclinations of
258 ca. 20° (Table 1 and Fig. 9). According to the strike of magnetic foliation, the majority
259 of sampling sites are characterized by NE-SW-striking and SE dipping magnetic
260 foliation, which are labeled as Group I (G-I; white stereographs in Fig. 9). Eleven
261 sites located in the central-southern part of the stock with depths greater than -670 m,
262 i.e. HSP16, HSP17, DTS18, DTS19, DGS20, HSP24, HSP25, DTS26, DTS27,
263 HSP32 and HSP37 are classified in Group II (G-II; grey stereographs in Fig. 9). The
264 sites in G-II display relatively consistent NW-SE-striking magnetic foliations and

265 steeper dipping angle than those in G-I (inserted stereographs in Fig. 10a and b). The
266 magnetic lineations of G-I are characterized by highly variable plunges with
267 directions sub-parallel or cross with the stock boundary (inserted stereograms in Fig.
268 10b). Especially, the sites of G-I lower than -670m show gentle to sub-horizontal
269 plunges of lineation (Fig. 10b). Nevertheless, the directions of magnetic lineation of
270 G-II show a consistent NW-SE trending and variable plunges (Fig. 10c and d).

271 **5.3. Whole-rock major and trace elements geochemistry**

272 Six fresh and representative samples for geochemical analysis were collected at
273 the -670m platform and sampling locations are the same as the AMS sampling (Fig.
274 11a). The acquired geochemical data and previous geochemical analysis are presented
275 in Table S1. Previous geochemical results of the Dongguashan stock are also included
276 in Table S1 for a comprehensive and comparative analysis (Wang et al., 2003, 2015,
277 Huang et al., 2004; Guo et al., 2013; Liu et al., 2018).

278 According to the SiO_2 content, the analyzed Dongguashan quartz diorites and
279 previous geochemical analysis present a wide range of SiO_2 (56.5% to 65.32 wt.%)
280 and the relatively low SiO_2 content Group II (G-II: 56.48 – 60 wt.%; Table S1 and Fig.
281 11). Moreover, G-I has a wider range of SiO_2 content than that of G-II (Fig. 11b-h).
282 The TiO_2 , Al_2O_3 , CaO , MgO , Na_2O and P_2O_5 display steadily decrease or constant
283 trend with increasing SiO_2 , suggesting that the minor compatible behavior (Fig.
284 11b-11g). K_2O shows constant or slightly increase in G-I with increasing SiO_2 (Fig.
285 11h), which may be due to the hydrothermal alteration during the subsequent
286 mineralization process.

287 **5.4. The 3D geometry of the stock and its related orebody**

288 The horizontal drilling sections and 3D geometry model of the Dongguashan
289 quartz diorite stock and related orebodies (Fig. 12) highlight several major features of
290 the Dongguashan quartz diorite stock. The stock has a complicated shape with a
291 principal NE-SW extending long axis. Many apophyses are formed within the strata
292 bedding (Fig. 12b, c and d) and the skarn orebodies are mainly developed in the
293 northern hinge and eastern limb of the Qingshanjiao anticline. The largest ore, i.e. the
294 Dongguashan ore, was yield between the Middle to Upper Carboniferous carbonates
295 and Upper Devonian sandstone with depth ranging from ca. -650 m to -850m (Fig.
296 12a), and the other two ore deposits, i.e. the Huashupo and Datuanshan ore deposits,
297 are localized along the contact zones of the Dongguashan stock (Fig. 12).

298 **6. Discussion**

299 **6.1. Significance of the petrofabric investigation**

300 The nature of the fabrics, i.e. whether primary or not, is pivotal for the
301 interpretation. Our microscopic petrographic investigations on the Dongguashan
302 quartz diorite and its country rocks show that the quartz diorite samples exhibit a
303 typical magmatic texture, and intrusion-related ductile deformation was absent in the
304 contact zone (Fig. 6). The dominantly low P_j values of the quartz diorite samples also
305 suggest that the stock has not been significantly affected by a subsequent regional
306 tectonic event (Hrouda and Lanza, 1989; Rochette et al., 1992). The ductile
307 deformation of the country rock of the Dongguashan quartz diorite stock is apparent
308 in folding and thrusting (Fig. 4f) that are considered to be inherited structures

309 resulting from the Triassic intracontinental event instead of resulted from magma
310 emplacement (Deng et al., 2011; Mao et al., 2011; Wang et al., 2011).

311 Moreover, our magnetic mineralogical analyses suggest that major magnetic
312 carriers of the Dongguashan quartz diorite are ferromagnetic and paramagnetic
313 minerals. According to the microscopic observations, the arrangement of the
314 magnetite and pyrrhotite is usually parallel to the long axis of the plagioclase and/or
315 biotite (Fig. 6e and 6f), indicating that the magnetic fabric ellipsoid is parallel to the
316 principal finite strain axes inferred from the petrographic fabric. Namely, the K1 and
317 K3 magnetic axes correspond to the mineral lineation and the foliation pole,
318 respectively. Consequently, we argue that the magnetic fabrics of the Dongguashan
319 quartz diorite revealed by our AMS investigation were primary fabric, which can be
320 used to reveal the magma emplacement process.

321 ***6.2. Interpretation of AMS results of the Dongguashan stock***

322 As mentioned above, the most remarkable feature of the AMS results of the
323 Dongguashan quartz diorite is the coexistence of two nearly orthogonal magnetic
324 fabric groups, i.e. G-I and G-II. Thus understanding of the magnetic fabric of the
325 Dongguashan quartz diorite stock is essential for the re-construction of the magma
326 emplacement process. The 3D geometry modelling of the Dongguashan quartz diorite
327 stock (Fig. 12) and a previous geobarometric study indicate that the stock has a small
328 volume and shallow emplacement depth (ca. 4-6 km; Du et al., 2004). Therefore, we
329 consider that the Dongguashan stock should be a rapidly emplaced and cooled stock,
330 in terms of previous studies on the duration of pluton construction (Matzel et al., 2006;

331 de Saint Blanquat et al., 2011). Consequently, this distinct magnetic fabric pattern
332 cannot be produced by magma convection in the magma chamber at emplacement
333 crust level, and detailed discussion of the AMS result is described below.

334 *6.2.1. AMS results for Group I*

335 Seventy-eight percent of the magnetic foliation of G-I is characterized by a
336 NE-SW strike with steep or high-angle southeastward dip (Fig. 10 and Table 1). This
337 pattern of relatively consistent strike and dip of the magnetic foliation in the
338 Dongguashan quartz diorite stock is different from previous AMS studies on other
339 stocks around the world, which usually present a circular array of inward dipping
340 magnetic foliations with strike parallel to the stock boundary (Cogné and Perroud,
341 1988; Hrouda and Lanza, 1989; Romeo et al., 2008; He et al., 2009; Piña et al., 2010).
342 Whereas the trend and plunge of magnetic lineation of these sites are highly variable
343 (Fig. 10c and 10d), which is a typical feature for the fabric developed in a stock
344 (Cogné and Perroud, 1988; Hrouda and Lanza, 1989; de Saint-Blanquat, et al., 2001).
345 This specific magnetic fabric pattern might be produced by the NW-SE directed
346 regional shortening setting or be affected by the pre-emplacement NE-SW-striking
347 structures in the country rocks. Nevertheless, previous studies suggest that the
348 Tongling Ore Cluster is mainly under extensional regime during the magma
349 emplacement epoch (e.g., Mao et al., 2003; Li et al., 2014). The petrographic
350 investigations on the stock and its country rocks also suggest that the Dongguashan
351 stock was not significantly influenced by any syn-magmatism and post-solidus
352 regional tectonics. Hence, these evidence seem to be inconsistent with the first

353 possibility. Alternatively, considering the parallelism between the pre-emplacment
354 fold and fault system developed in the country rocks and the NE-SW-striking
355 magnetic foliation, we propose that these pre-emplacment structures may serve as
356 magma ascent paths to form the NE-SW trending steep magnetic foliations, thus the
357 magma ascent was principally driven by its buoyancy (Marsh, 1982; Clark et al., 1998;
358 Paterson and Jr, 1993).

359 In particular, there are seven sites located at depths of -730m, -790m, and -850m
360 of G-I show the strike of magnetic foliation crosscutting the stock boundary with
361 mainly sub-vertical to northward dip (Fig. 10a). The magnetic lineation is mainly
362 trending NE-SW or E-W with sub-horizontal plunges. This phenomenon may be due
363 to the boundary effect, complex magma flow or magma outflow (e.g., Ferré et al.,
364 2002; Kratinová et al., 2006). The borehole data also confirms that the Dongguashan
365 quartz diorite intrusion was intruded into the stratigraphic interface at these depths
366 (Fig. 12; Liu et al., 2014).

367 6.2.2. AMS results for Group II

368 The magnetic fabric of G-II is characterized by consistent NW-SE-striking
369 magnetic foliation and lineation, and this preferred orientation is roughly
370 perpendicular to those of G-I and the NE-SW-striking regional structures. In addition,
371 we have observed pervasively developed NW-SE striking fractures, calcite veins and
372 vein-type orebodies in the Dongguashan stock and its country rocks (Fig. 5), which
373 are parallel to the strike of the magnetic fabric of G-II. The NW-SE oriented magnetic
374 fabrics, fractures and veins may be produced either by regional shortening in NW-SE

375 direction, or the magma was intruded into the NW-SE striking brittle structures, which
376 produced by the overall extension of the upper crust in the Early Cretaceous epoch.
377 However, contemporaneous Early Cretaceous magmatism is widely developed in the
378 TOC, which is usually display a high-k and calc-alkaline affinity and considered to be
379 a consequence of the regional extension (Wang et al., 2003; Wu et al., 2010; Guo et al.,
380 2013; Zhou et al., 2015). Therefore, the hypothesis of the regional shortening is not
381 preferred, we thus propose that the G-II magma emplacement was affected by overall
382 extension of the upper crust.

383 ***6.3. Overview of research and tentative magma emplacement model proposal***

384 Apart from the difference in the AMS results, a sharp intrusive contact was
385 observed at -670 m platform (Fig. 13), suggesting that the Dongguashan was
386 constructed by multiple magma pulses. In addition, this and previous geochemical
387 studies on the Dongguashan quartz diorite stock show that the major elements have a
388 wide composition range (Fig. 11 and Table S1), which may result from fractional
389 crystallization or multiple magma pulses emplacement model. Although the major
390 elements seem to be distributed along a regression line, whereas the higher SiO₂
391 content samples were collected from the outer and deeper parts of the stock compared
392 with the less silica-rich samples (Fig. 11). This distribution opposes the normal
393 fractional crystallization trend in a gradual cooling magma chamber (Tindle and
394 Pearce, 1981; McNulty et al., 2000; Coleman et al., 2004). Gradual petrological
395 change or composition zoning related to fractional crystallization is also absent in the
396 stock. Therefore, the fractional crystallization process seems not suitable to explain

397 the composition variation of the Dongguashan stock. Furthermore, previous
398 geochronological studies in the Shizishan orefield also present a wide age spectrum,
399 indicating a relatively long time magma emplacement process (Wu et al., 2010; Yang
400 and Lee, 2011; Guo et al., 2013; Wang et al., 2015; Liu et al., 2018). In summary, all
401 these evidence suggest that the Dongguashan quartz diorite stock was constructed by
402 multiple magma pulses, and a two-stage magma emplacement model is proposed for
403 the Dongguashan quartz diorite stock as described below.

404 On account of the samples of G-I are located in the outer part of the stock from
405 -850m to -390m, and the samples of G-II are collected in the inner part of the stock
406 with depths lower than -650 m. Moreover, the strike of magnetic foliation of G-I is cut
407 by the G-II (Fig. 10). Therefore, we suggest that G-I and G-II belongs to the earlier
408 and late magma pulses emplacement stages, respectively.

409 First, the initial magma emplacement occurred when the internal buoyancy
410 force of the deeply seated magma chamber exceeded the lithostatic pressure of the
411 country rocks (Fig. 14a; van der Molen and Paterson, 1979; Bachmann and Bergantz,
412 2004; Vigneresse, 2007). Previous studies suggest the existence of NE-SW-striking
413 basement faults in the crust, and the upper crust was deformed by Triassic
414 pre-emplacement regional tectonics (Deng et al., 2006), which yielded paths or
415 channels for the magma ascent (Fig. 14a). The decollement of country rocks produced
416 part of the space for magma emplacement (Fig. 4f). Moreover, the abundance of
417 xenoliths observed in the stock boundary suggests that the space for magma
418 emplacement was partly created by magma stoping (Marsh, 1982; Clark et al., 1998).

419 The relatively more regular stock boundary in the western side of the stock than in the
420 eastern one suggests an eastward magma accretion trend. The dilation (possibly
421 controlled by hydrothermal fluids), inflation and uplifting of the brittle country rocks
422 accommodated the gradual emplacement of magma (Fig. 14b).

423 Second, the consistent NW-SE-striking magnetic foliation of Group II samples
424 and its parallelism with the NW-SE-striking fractures developed in the stock and
425 country rocks, which produced by the regional extension, suggest that the
426 emplacement of the late magma pulse was strongly controlled by these fractures (Fig.
427 14c).

428 ***6.4. Implications for the associated orebody localization***

429 Our study reveals that the Dongguashan stock was constructed by at least two
430 magma pulses. Discontinuous magma emplacement changes the temperature field,
431 fluid composition, oxygen fugacity and elements partition coefficients, and therefore
432 is an important mechanism for the formation of huge intrusion related ore deposits
433 (e.g., Holzheid and Lodders, 2001; Vigneresse, 2007; Huber et al., 2012;
434 Chelle-Michou et al., 2015).

435 According to the restored 3D stock and orebody geometry model, the largest ore
436 reserves are located at the Devonian-Carboniferous (D-C) stratigraphic interface with
437 depth between ca. -650 and -950 m (Fig. 12). The occurrence of these stratiform
438 orebodies is consistent with the flanks of the Qingshanjiao anticline, denoting that the
439 hydrothermal fluid was intruded along the strata interface (Tang et al., 1998). The
440 AMS results of the sites close to the stock boundary at depths of -670 to -850 m

441 suggest that magma outflow occurred within these strata, which is also supported by
442 tiny and rootless granitic body revealed by borehole data (Fig. 12). Previous
443 geochemical studies also suggest that the magma is the dominant source of
444 ore-forming fluid. Thus, the stratiform skarn orebodies were mainly yielded by the
445 early emplaced magma pulse, which was emplaced along pre-emplacment structures
446 or discontinuous mechanical interfaces in the country rocks.

447 The second orebody localization zone concerns the contact zone between the
448 stock and country rock. This includes the Huashupo and Datuanshan skarn-type
449 orebodies, which are developed at the eastern side of the stock at depths of -300 to
450 -600 m, and thus are related to the earlier emplaced magma pulse (Fig. 12). According
451 to our study, the Dongguashan stock was constructed by successive magma pulses
452 with an eastward accretion trend and forceful-like emplacement behavior. Thus, the
453 country rock in the eastern side of the stock has a higher degree of deformation,
454 intense fracturing and higher permeability and temperature, which were produced by
455 the repeated magma intrusion. In addition, the restored 3D geometrical model shows
456 that the occurrence of the orebody in the eastern side of the stock is roughly parallel to
457 the stock-country rock contact surface, which dips gently outward in contrast to a
458 sub-vertical contact in the western side (Fig. 12). Consequently, we propose that
459 different interaction between the magma and country rock may affect the localization
460 of the orebodies.

461 The third type of orebody, i.e. the vein-like and veinlet-disseminated orebodies,
462 is widely developed inside the Dongguashan stock and partly developed in the

463 NW-SE-striking fractures (Fig. 5c and 5d). The parallelism among the ore veins, the
464 strike of magnetic foliation of G-II and the fractures (Figs. 5 and 12) suggests that the
465 space for the vein-like orebody was controlled by the later magma pulse.

466 **7. Conclusions**

467 According to our macro- and microscopic observations, geochemical and AMS
468 analyses and 3D geometrical modelling of the Dongguashan stock, we concluded that:

469 1) The Dongguashan stock was constructed by at least two stages magma
470 emplacement. The AMS results of these two magma stages can also be divided into
471 two groups, i.e. G-I and G-II, corresponding to earlier and later magma pulses,
472 respectively. G-I is dominated by a NE-SW striking magnetic foliation, which is
473 parallel to the trend of the pre-emplacment folds and faults, suggesting that the
474 magma emplacement was probably affected by the pre-emplacement structure. G-II is
475 characterized by a NW-SE-striking magnetic foliation, which is parallel to the
476 regional extensional structures, suggesting the control of regional extension on
477 magma emplacement.

478 2) The 3D geometrical modelling of the stock presents a triangular shape with
479 irregular and bulged boundary in the eastern side of the stock, denoting that the stock
480 was constructed by an eastward magma accretion.

481 3) The AMS results suggest that the magma was intruded into the strata
482 interface at depths between -670 to -850 m, which is the essential factor for the
483 formation of the stratiform ore deposit in the Dongguashan area. Moreover, the
484 eastward magma accretion resulting in highly fractured and more permeable country

485 rocks in the eastern stock contact zone that can explain why the skarn orebodies are
486 localized in the eastern stock contact zone. The NW-SE-striking ore veins were likely
487 controlled by the emplacement of the late magma pulse under an extensional regional
488 tectonic setting.

489 **Acknowledgements**

490 We thank Mr. Wangsheng Jiang, Hui Jin, Yong Jiang (Tongling Nonferrous
491 Metals Group Holdings Company) for their help in sample collection. Our thanks also
492 go to Mrs. Xinxin Sun for her help in magnetic mineralogical analysis, and Jeffrey M.
493 Dick for language editing. Moreover, detailed language editing and constructive
494 suggestions on the first manuscript version from the associate editor Prof. Deru Xu
495 was highly appreciated. We also appreciate the pertinent comments and constructive
496 suggestions provided by Dr. Wei Wei and another two anonymous reviewers that have
497 significantly improved the presentation of this study. Access to the Dongguashan mine
498 and offering of borehole data by the Tongling Nonferrous Metals Group Holdings
499 Company are highly appreciated. We also appreciate financial support from the
500 National Natural Science Foundation of China (41372338, 41772351 and 41902209)
501 and Research foundation of Hunan Province (2019JJ50832), French LABEX
502 VOLTAIRE (ANR-10-LABX-100-01) and EQUIPEX PLANET
503 (ANR-11-EQPX-0036).

504 **References**

505 Améglio, L., Vignerresse, J.L. and Bouchez, J.L., 1997. Granite Pluton Geometry and
506 Emplacement Mode Inferred from Combined Fabric and Gravity Data. In: J.L.

- 507 Bouchez, D.H.W. Hutton and W.E. Stephens (Editors), Granite: From Segregation
508 of Melt to Emplacement Fabrics. Springer Netherlands, Dordrecht, pp. 199-214.
509 https://doi.org/10.1007/978-94-017-1717-5_13
- 510 Bachmann O, Bergantz GW. On the Origin of Crystal-poor Rhyolites: Extracted from
511 Batholithic Crystal Mushes. Journal of Petrology.
512 2004;45:1565-82.<http://dx.doi.org/10.1093/petrology/egh019>.
- 513 Blevin PL. Redox and Compositional Parameters for Interpreting the Granitoid
514 Metallogeny of Eastern Australia: Implications for Gold-rich Ore Systems.
515 Resource Geology. 2004;54:241-52.
516 <https://doi.org/10.1111/j.1751-3928.2004.tb00205.x>.
- 517 Borradaile GJ. Magnetic susceptibility, petrofabrics and strain. Tectonophysics.
518 1988;156:1-20. [https://doi.org/10.1016/0040-1951\(88\)90279-X](https://doi.org/10.1016/0040-1951(88)90279-X).
- 519 Borradaile G.J., Jackson M. Anisotropy of magnetic susceptibility (AMS): magnetic
520 petrofabrics of deformed rocks. In: In: Martín-Hernández, F., Lüneburg, C.M.,
521 Aubourg, C., Jackson, M. (Eds.), Magnetic Fabric: Methods and Applications,
522 2004. vol. 238. Geological Society, London, Special Publications, pp. 299–360.
- 523 Bouchez JL. Granite is Never Isotropic: An Introduction to AMS Studies of Granitic
524 Rocks. In: Bouchez JL, Hutton DHW, Stephens WE, editors. Granite: From
525 Segregation of Melt to Emplacement Fabrics. Dordrecht: Springer Netherlands;
526 1997. p. 95-112. https://doi.org/10.1007/978-94-017-1717-5_6
- 527 Candela PA, Piccoli PM, Hedenquist JW, Thompson JFH, Goldfarb RJ, Richards JP.
528 Magmatic Processes in the Development of Porphyry-Type Ore Systems. One

- 529 Hundredth Anniversary Volume: Society of Economic Geologists; 2005. p. 0.
530 <https://doi.org/10.5382/av100.03>
- 531 Cao W, Liu L, Liu H, Lai F. Investigating the Irregular Localization of Skarn
532 Orebodies by Computational Modeling in the Fenghuangshan Ore Field,
533 Tongling District, Anhui Province, China. *Natural Resources Research*. 2020.
534 <http://dx.doi.org/10.1007/s11053-020-09655-x>.
- 535 Cao Y, Du Y, Gao F, Hu L, Xin F, Pang Z. Origin and evolution of hydrothermal fluids
536 in the Taochong iron deposit, Middle–Lower Yangtze Valley, Eastern China:
537 Evidence from microthermometric and stable isotope analyses of fluid inclusions.
538 *Ore Geology Reviews*. 2012;48:225–38.
539 <http://dx.doi.org/10.1016/j.oregeorev.2012.03.009>.
- 540 Cao Y, Du Y, Pang Z, Ren C, Du Y, Xiao F, Zhou G, Chen J. Sulfide zonal texture and
541 its geological significance of ores from the Dongguashan copper (gold) deposit in
542 Tongling, Anhui Province, China. *Acta Petrologica Sinica*. 2016;32(2):334–350
543 (in Chinese with English abstract).
- 544 Chang Y, Liu P, Wu C. The copper-iron belt of the lower and middle reaches of the
545 Changjiang river. 1991. Geological Publishing House, Beijing, pp. 1–379 (in
546 Chinese with English abstract).
- 547 Chelle-Michou C, Chiaradia M, Béguelin P, Ulianov A. Petrological Evolution of the
548 Magmatic Suite Associated with the Coroccohuayco Cu(–Au–Fe)
549 Porphyry–Skarn Deposit, Peru. *Journal of Petrology*.
550 2015;56:1829–62.<http://dx.doi.org/10.1093/petrology/egv056>.

- 551 Chen Y, Nabelek PI. The influences of incremental pluton growth on magma
552 crystallinity and aureole rheology: numerical modeling of growth of the Papoose
553 Flat pluton, California. *Contributions to Mineralogy and Petrology*.
554 2017;172.<http://dx.doi.org/10.1007/s00410-017-1405-6>.
- 555 Chen YJ, Pirajno F, Wu G, Qi JP, Xiong XL. Epithermal deposits in North Xinjiang,
556 NW China. *International Journal of Earth Sciences*.
557 2012;101:889-917.<http://dx.doi.org/10.1007/s00531-011-0689-4>.
- 558 Chesley JT, Halliday AN, Snee LW, Mezger K, Shepherd TJ, Scrivener RC.
559 Thermochronology of the Cornubian batholith in southwest England:
560 Implications for pluton emplacement and protracted hydrothermal mineralization.
561 *Geochimica et Cosmochimica Acta*. 1993;57:1817-35.
562 [https://doi.org/10.1016/0016-7037\(93\)90115-D](https://doi.org/10.1016/0016-7037(93)90115-D).
- 563 Clarke DB, Henry AS, White MA. Exploding xenoliths and the absence of 'elephants'
564 graveyards' in granite batholiths. *Journal of Structural Geology*. 1998;20:1325-43.
565 [https://doi.org/10.1016/S0191-8141\(98\)00082-0](https://doi.org/10.1016/S0191-8141(98)00082-0).
- 566 Cogné J-P, Perroud H. Anisotropy of magnetic susceptibility as a strain gauge in the
567 Flamanville granite, NW France. *Physics of the Earth and Planetary Interiors*.
568 1988;51:264-70.[http://dx.doi.org/10.1016/0031-9201\(88\)90068-4](http://dx.doi.org/10.1016/0031-9201(88)90068-4).
- 569 Coleman DS, Gray W, Glazner AF. Rethinking the emplacement and evolution of
570 zoned plutons: Geochronologic evidence for incremental assembly of the
571 Tuolumne Intrusive Suite, California. *Geology*. 2004;32:433.
572 <http://dx.doi.org/10.1130/g20220.1>.

- 573 de Saint Blanquat M, Horsman E, Habert G, Morgan S, Vanderhaeghe O, Law R, et al.
574 Multiscale magmatic cyclicality, duration of pluton construction, and the
575 paradoxical relationship between tectonism and plutonism in continental arcs.
576 *Tectonophysics*. 2011;500:20-33.<http://dx.doi.org/10.1016/j.tecto.2009.12.009>.
- 577 de Saint-Blanquat M, Law RD, Bouchez J-L, Morgan SS. Internal structure and
578 emplacement of the Papoose Flat pluton: An integrated structural, petrographic,
579 and magnetic susceptibility study. *GSA Bulletin*.
580 2001;113:976-95.[http://dx.doi.org/10.1130/0016-7606\(2001\)113<0976:isaet>2.0](http://dx.doi.org/10.1130/0016-7606(2001)113<0976:isaet>2.0)
581 [.co;2](http://dx.doi.org/10.1130/0016-7606(2001)113<0976:isaet>2.0).
- 582 Deng J, Wang Q, Huang D, Wan L, Yang L, Gao B. Transport network and flow
583 mechanism of shallow ore-bearing magma in Tongling ore cluster area. *Science*
584 *in China Series D*.
585 2006;49:397-407.<http://dx.doi.org/10.1007/s11430-006-0397-2>.
- 586 Deng J, Wang Q, Xiao C, Yang L, Liu H, Gong Q, et al.
587 Tectonic-magmatic-metallogenic system, Tongling ore cluster region, Anhui
588 Province, China. *International Geology Review*. 2011;53:449-76.
589 <http://dx.doi.org/10.1080/00206814.2010.501538>
- 590 Du Y. Petrological and mineralogical study of enclaves in plutons in the typical
591 mining districts of Tongling, Anhui and its bearing on the process of
592 magmatism-metallogeny. *Chinese Journal of Geochemistry*. 1999;18:208.
593 <http://dx.doi.org/10.1007/BF02831066>.
- 594 Dunlop DJ, Özdemir Ö. *Rock Magnetism: Fundamentals and Frontiers*. Cambridge:

- 595 Cambridge University Press; 1997. [http://dx.doi.org/](http://dx.doi.org/10.1017/CBO9780511612794)
596 10.1017/CBO9780511612794
- 597 Duuring P, Hagemann SG. A thrust ramp model for gold mineralization at the archean
598 Trondhjemite-hosted Tarmoola deposit: The importance of heterogeneous stress
599 distributions around granitoid contacts. *Econ Geol Bull Soc Econ Geol.*
600 2001;96:1379-96. <http://dx.doi.org/10.2113/96.6.1379>.
- 601 Eldursi K, Branquet Y, Guillou-Frottier L, Marcoux E. Numerical investigation of
602 transient hydrothermal processes around intrusions: Heat-transfer and
603 fluid-circulation controlled mineralization patterns. *Earth and Planetary Science*
604 *Letters.* 2009;288:70-83. <http://dx.doi.org/10.1016/j.epsl.2009.09.009>.
- 605 Ernst RE, Baragar WRA. Evidence from magnetic fabric for the flow pattern of
606 magma in the Mackenzie giant radiating dyke swarm. *Nature.* 1992;356:511-3.
607 <http://dx.doi.org/10.1038/356511a0>.
- 608 Eugster HP. Granites and hydrothermal ore deposits: a geochemical framework.
609 *Mineralogical Magazine.* 2018;49:7-23.
610 <http://dx.doi.org/10.1180/minmag.1985.049.350.02>.
- 611 Ferré EC, Geissman JW, Chauvet A, Vauchez A, Zechmeister MS. Focal mechanism
612 of prehistoric earthquakes deduced from pseudotachylyte fabric. *Geology.*
613 2015;43:531-4. <http://dx.doi.org/10.1130/g36587.1>.
- 614 Gu L, Wu C, Zhang Z, Pirajno F, Pei N, Chen P, et al. Comparative study of
615 re-forming fluids of hydrothermal copper-gold deposits in the Lower Yangtze
616 River Valley, China. *Int Geol Rev. International Geology Review.*

- 617 2011;53:477-98.
- 618 Guo W, Lu J, Jiang S, Zhang R, Zhao Z. Chronology, Hf isotopes, geochemistry, and
619 petrogenesis of the magmatic rocks in the Shizishan ore field of Tongling, Anhui
620 Province. *Science China Earth Sciences*.
621 2013;56:993-1013.<http://dx.doi.org/10.1007/s11430-013-4589-2>.
- 622 He B, Xu Y-G, Paterson S. Magmatic diapirism of the Fangshan pluton, southwest of
623 Beijing, China. *Journal of Structural Geology*. 2009;31:615-26.
624 <https://doi.org/10.1016/j.jsg.2009.04.007>.
- 625 Hedenquist JW, Lowenstern JB. The role of magmas in the formation of hydrothermal
626 ore deposits. *Nature*. 1994;370:519.<http://dx.doi.org/10.1038/370519a0>.
- 627 Heinrich CA, Walshe JL, Harrold BP. Chemical mass transfer modelling of
628 ore-forming hydrothermal systems: current practise and problems. *Ore Geology
629 Reviews*. 1996b;10:319-38. [https://doi.org/10.1016/0169-1368\(95\)00029-1](https://doi.org/10.1016/0169-1368(95)00029-1).
- 630 Holwell DA, Keays RR, Firth EA, Findlay J. Geochemistry and Mineralogy of
631 Platinum Group Element Mineralization in the River Valley Intrusion, Ontario,
632 Canada: A Model for Early-Stage Sulfur Saturation and Multistage Emplacement
633 and the Implications for “Contact-Type” Ni-Cu-PGE Sulfide Mineralization*.
634 *Economic Geology*. 2014;109:689-712.
635 <http://dx.doi.org/10.2113/econgeo.109.3.689>.
- 636 Holzheid A, Lodders K. Solubility of copper in silicate melts as function of oxygen
637 and sulfur fugacities, temperature, and silicate composition. *Geochimica et
638 Cosmochimica Acta*. 2001;65:1933-51.

- 639 [https://doi.org/10.1016/S0016-7037\(01\)00545-2](https://doi.org/10.1016/S0016-7037(01)00545-2).
- 640 Hrouda F. Magnetic anisotropy of rocks and its application in geology and geophysics.
641 Geophysical surveys. 1982;5:37-82.<http://dx.doi.org/10.1007/BF01450244>.
- 642 Hrouda Fe, Lanza R. Magnetic fabric in the Biella and Traversella stocks (Periadriatic
643 Line) : implications for the mode of emplacement. Physics of the Earth and
644 Planetary Interiors.
645 1989;56:337-48.[https://doi.org/10.1016/0031-9201\(89\)90168-4](https://doi.org/10.1016/0031-9201(89)90168-4).
- 646 Hua R, Chen P, Zhang W, Lu J. Three major metallogenic events in Mesozoic in
647 South China. Mineral deposits. 2005;24:99-107.
- 648 Huang S, Xu Z, Gu L. A discussion on geochemical characteristics and genesis of
649 intrusions in Shizishan orefield, Tongling area, Anhui Province. Geol. J. China
650 Univ. 2004;10 (2), 217–226 (in Chinese with English abstract).
- 651 Huber C, Bachmann O, Vigneresse J-L, Dufek J, Parmigiani A. A physical model for
652 metal extraction and transport in shallow magmatic systems. Geochemistry,
653 Geophysics, Geosystems. 2012;13.<http://dx.doi.org/10.1029/2012GC004042>.
- 654 Jelínek V, Kropáček V. Statistical processing of anisotropy of magnetic susceptibility
655 measured on groups of specimens. Studia Geophysica et Geodaetica.
656 1978;22:50-62.<http://dx.doi.org/10.1007/BF01613632>.
- 657 Jelínek V. Characterization of the magnetic fabric of rocks. Tectonophysics.
658 1981;79:T63-T7. [https://doi.org/10.1016/0040-1951\(81\)90110-4](https://doi.org/10.1016/0040-1951(81)90110-4).
- 659 Kratinová Z, Závada P, Hrouda F, Schulmann K. Non-scaled analogue modelling of
660 AMS development during viscous flow: A simulation on diapir-like structures.

- 661 Tectonophysics. 2006;418:51-61.<http://dx.doi.org/10.1016/j.tecto.2005.12.013>.
- 662 Lai JQ, Chi GX, Peng SL, Shao YJ, Yang B. Fluid Evolution in the Formation of the
663 Fenghuangshan Cu-Fe-Au Deposit, Tongling, Anhui, China. *Economic Geology*.
664 2007;102:949-70. <http://dx.doi.org/10.2113/gsecongeo.102.5.949>
- 665 Li H, Zhang H, Ling M-X, Wang F-Y, Ding X, Zhou J-B, et al. Geochemical and
666 zircon U–Pb study of the Huangmeijian A-type granite: implications for
667 geological evolution of the Lower Yangtze River belt. *International Geology*
668 *Review*. 2011;53:499-525.<http://dx.doi.org/10.1080/00206814.2010.496202>.
- 669 Li J, Zhang Y, Dong S, Johnston ST. Cretaceous tectonic evolution of South China: A
670 preliminary synthesis. *Earth-Science Reviews*. 2014;134:98-136.
671 <https://doi.org/10.1016/j.earscirev.2014.03.008>.
- 672 Li Y, Li Q-L, Yang J-H. Tracing water-rock interaction in carbonate replacement
673 deposits: A SIMS pyrite S-Pb isotope perspective from the Chinese Xinqiao
674 system. *Ore Geology Reviews*. 2019;107:248-57.
675 <https://doi.org/10.1016/j.oregeorev.2019.02.022>.
- 676 Liang Q, Jing H, Gregoire DC. Determination of trace elements in granites by
677 inductively coupled plasma mass spectrometry. *Talanta*. 2000;51:507-13.
678 [https://doi.org/10.1016/S0039-9140\(99\)00318-5](https://doi.org/10.1016/S0039-9140(99)00318-5).
- 679 Lin J-l, Fuller M, Zhang W-y. Preliminary Phanerozoic polar wander paths for the
680 North and South China blocks. *Nature*. 1985;313:444-9.
681 <http://dx.doi.org/10.1038/313444a0>.
- 682 Liu G, Yuan F, Deng Y, Wang F, White NC, Huizenga JM, et al. Ore-fluid

- 683 geochemistry of the Hehuashan Pb–Zn deposit in the Tongling ore district, Anhui
684 province, China: Evidence from REE and C–H–O isotopes of calcite. *Ore*
685 *Geology Reviews*. 2019;103279.
686 <https://doi.org/10.1016/j.oregeorev.2019.103279>.
- 687 Liu L, Wan C, Zhao C, Zhao Y. Geodynamic constraints on orebody localization in
688 the Anqing orefield, China: Computational modeling and facilitating predictive
689 exploration of deep deposits. *Ore Geology Reviews*. 2011;43:249-63.
690 <https://doi.org/10.1016/j.oregeorev.2011.09.005>
- 691 Liu L, Zhao Y, Sun T. 3D computational shape- and cooling process-modeling of
692 magmatic intrusion and its implication for genesis and exploration of
693 intrusion-related ore deposits: An example from the Yueshan intrusion in Anqing,
694 China. *Tectonophysics*.
695 2012;526-529:110-23. <https://doi.org/10.1016/j.tecto.2011.09.006>.
- 696 Liu LM, Sun T, Zhou RC. Epigenetic genesis and magmatic intrusion's control on the
697 Dongguashan stratabound Cu–Au deposit, Tongling, China: Evidence from field
698 geology and numerical modeling. *Journal of Geochemical Exploration*.
699 2014;144:97-114. <https://doi.org/10.1016/j.gexplo.2014.03.008>
- 700 Liu Z-f, Shao Y-j, Wang C, Liu Q-q. Genesis of the Dongguashan skarn Cu-(Au)
701 deposit in Tongling, Eastern China: Evidence from fluid inclusions and H-O-S-Pb
702 isotopes. *Ore Geology Reviews*. 2018.
703 <https://doi.org/10.1016/j.oregeorev.2018.11.021>.
- 704 Lu JJ, Hua RM, Xu ZW. A two-stage model for formation of the Dongguashan Cu-Au

- 705 deposit. *Geological Journal of China Universities*. 2003;9:678-90.
- 706 Lü Q, Qi G, Yan J. 3D geologic model of Shizishan ore field constrained by gravity
707 and magnetic interactive modeling: A case history. *Geophysics*.
708 2013;78:B25-B35.
- 709 Lü QT, Shi DN, Liu ZD, Zhang YQ, Dong SW, Zhao JH. Crustal structure and
710 geodynamics of the Middle and Lower reaches of Yangtze metallogenic belt and
711 neighboring areas: Insights from deep seismic reflection profiling. *Journal of*
712 *Asian Earth Sciences*.
713 2015;114:704-16.<http://dx.doi.org/10.1016/j.jseaes.2015.03.022>.
- 714 Mao J, Li XF, Zhang ZH, Wang Y, Li HM, Hu HB. Geology, distribution, types and
715 tectonic settings of Mesozoic epithermal gold deposits in East China. *Geological*
716 *Journal of China Universities*. 2003;9:620-37.
- 717 Mao J, Xie G, Duan C, Pirajno F, Ishiyama D, Chen Y. A tectono-genetic model for
718 porphyry-skarn-stratabound Cu-Au-Mo-Fe and magnetite-apatite deposits
719 along the Middle-Lower Yangtze River Valley, Eastern China. *Ore Geology*
720 *Reviews*. 2011;43:294-314.<https://doi.org/10.1016/j.oregeorev.2011.07.010>.
- 721 Mao JW, Xie GQ, Guo CL, Yuan SD, Cheng YB, Chen YC. Spatial-temporal
722 distribution of Mesozoic ore deposits in South China and their metallogenic
723 settings. *Geological Journal of China Universities*. 2008;14:510-26.
- 724 Marsh BD. On the mechanics of igneous diapirism, stoping, and zone melting.
725 *American Journal of Science*.
726 1982b;282:808.<http://dx.doi.org/10.2475/ajs.282.6.808>.

- 727 Matzel JEP, Bowring SA, Miller RB. Time scales of pluton construction at differing
728 crustal levels: Examples from the Mount Stuart and Tenpeak intrusions, North
729 Cascades, Washington. GSA Bulletin.
730 2006;118:1412-30.<http://dx.doi.org/10.1130/B25923.1>.
- 731 McNulty BA, Tobisch OT, Cruden AR, Gilder S. Multistage emplacement of the
732 Mount Givens pluton, central Sierra Nevada batholith, California. Geological
733 Society of America Bulletin.
734 2000;112:119-35.[http://dx.doi.org/10.1130/0016-7606\(2000\)112<119:meotmg>2.0.co;2](http://dx.doi.org/10.1130/0016-7606(2000)112<119:meotmg>2.0.co;2).
- 735 0.co;2.
- 736 Pan Y, Dong P. The Lower Changjiang (Yangzi/Yangtze River) metallogenic belt, east
737 central China: intrusion- and wall rock-hosted Cu–Fe–Au, Mo, Zn, Pb, Ag
738 deposits. Ore Geology Reviews. 1999;15:177-242.
739 [http://dx.doi.org/10.1016/S0169-1368\(99\)00022-0](http://dx.doi.org/10.1016/S0169-1368(99)00022-0).
- 740 Paterson SR, Jr TKF. Re-examining pluton emplacement processes. Journal of
741 Structural Geology. 1993;15:191-206.
742 [https://doi.org/10.1016/0191-8141\(93\)90095-R](https://doi.org/10.1016/0191-8141(93)90095-R)
- 743 Piña R, Romeo I, Ortega L, Lunar R, Capote R, Gervilla F, et al. Origin and
744 emplacement of the Aguablanca magmatic Ni-Cu-(PGE) sulfide deposit, SW
745 Iberia: A multidisciplinary approach. Geological Society of America Bulletin.
746 2010;122:915-25.<http://dx.doi.org/10.1130/b30046.1>.
- 747 Reynolds RR. Factors controlling the localization of ore deposits in the Shullsburg
748 area, Wisconsin-Illinois zinc-lead district. Economic Geology.

- 749 1958;53:141-63.<http://dx.doi.org/10.2113/gsecongeo.53.2.141>.
- 750 Rochette P, Jackson M, Aubourg C. Rock magnetism and the interpretation of
751 anisotropy of magnetic susceptibility. *Reviews of Geophysics*.
752 1992;30:209-26.<http://dx.doi.org/10.1029/92RG00733>.
- 753 Romeo I, Tejero R, Capote R, Lunar R. 3D gravity modelling of the Aguablanca
754 Stock, tectonic control and emplacement of a Variscan gabbro-norite bearing a
755 Ni-Cu-PGE ore, SW Iberia. *Geological Magazine*.
756 2008;145:345-59.<http://dx.doi.org/10.1017/s0016756808004470>.
- 757 Schöpa A, Annen C, Dilles J, Blundy J, Sparks S. Magma Emplacement Rates and
758 Porphyry Copper Deposits: Thermal Modeling of the Yerington Batholith,
759 Nevada. *Economic Geology*. 2017;112:1653-72.
760 <http://dx.doi.org/10.5382/econgeo.2017.4525>.
- 761 Shi D, Lü Q, Xu W, Yan J, Zhao J, Dong S, et al. Crustal structure beneath the
762 middle–lower Yangtze metallogenic belt in East China: Constraints from passive
763 source seismic experiment on the Mesozoic intra-continental mineralization.
764 *Tectonophysics*. 2013;606:48-59.<http://dx.doi.org/10.1016/j.tecto.2013.01.012>.
- 765 Sillitoe RH. Porphyry Copper Systems*. *Economic Geology*.
766 2010;105:3-41.<http://dx.doi.org/10.2113/gsecongeo.105.1.3>.
- 767 Sun W, Ding X, Hu Y-H, Li X-H. The golden transformation of the Cretaceous plate
768 subduction in the west Pacific. *Earth and Planetary Science Letters*.
769 2007;262:533-42.<http://dx.doi.org/10.1016/j.epsl.2007.08.021>.
- 770 Tang YC, Wu YC, Chu GZ, Xing FM, Wang YM, Cao FY, Chang YF. Geology of

- 771 copper-gold polymetallic deposits in the Along-Changjiang area of Anhui
772 Province. Geological Publishing House, Beijing, 1998; pp. 1–351 (in Chinese
773 with English abstract).
- 774 Tarling D, Hrouda F. Magnetic anisotropy of rocks: Springer Science & Business
775 Media; 1993.
- 776 Thompson JFH, Sillitoe RH, Baker T, Lang JR, Mortensen JK. Intrusion-related gold
777 deposits associated with tungsten-tin provinces. *Mineralium Deposita*.
778 1999;34:323-34.<http://dx.doi.org/10.1007/s001260050207>.
- 779 Tindle AG, Pearce JA. Petrogenetic modelling of in situ fractional crystallization in
780 the zoned Loch Doon pluton, Scotland. *Contributions to Mineralogy and
781 Petrology*. 1981;78:196-207.<http://dx.doi.org/10.1007/BF00373781>.
- 782 van der Molen I, Paterson MS. Experimental deformation of partially-melted granite.
783 *Contributions to Mineralogy and Petrology*.
784 1979;70:299-318.<http://dx.doi.org/10.1007/BF00375359>.
- 785 Vigneresse J-L. Element Mobility in Melts during Successive Intrusions of
786 Crustal-derived Magmas and Sn-W Mineralization. *Resource Geology*.
787 2006;56:293-314.<http://dx.doi.org/10.1111/j.1751-3928.2006.tb00285.x>.
- 788 Vigneresse JL. The role of discontinuous magma inputs in felsic magma and ore
789 generation. *Ore Geology Reviews*. 2007;30:181-216.
790 <https://doi.org/10.1016/j.oregeorev.2006.03.001>.
- 791 Wang Q, Deng J, Huang D, Xiao C, Yang L, Wang Y. Deformation model for the
792 Tongling ore cluster region, east-central China. *International Geology Review*.

- 793 2011;53:562-79.<http://dx.doi.org/10.1080/00206814.2010.496236>.
- 794 Wang Q, Xu J-F, Zhao Z-H, Bao Z-W, Xu W, Xiong X-L. Cretaceous high-potassium
795 intrusive rocks in the Yueshan-Hongzhen area of east China: Adakites in an
796 extensional tectonic regime within a continent. *GEOCHEMICAL JOURNAL*.
797 2004;38:417-34.<http://dx.doi.org/10.2343/geochemj.38.417>.
- 798 Wang S-W, Zhou T-F, Yuan F, Fan Y, Zhang L-J, Song Y-L. Petrogenesis of
799 Dongguashan skarn-porphyry Cu-Au deposit related intrusion in the Tongling
800 district, eastern China: Geochronological, mineralogical, geochemical and Hf
801 isotopic evidence. *Ore Geology Reviews*.
802 2015;64:53-70.<http://dx.doi.org/10.1016/j.oregeorev.2014.06.012>.
- 803 Wei W, Martelet G, Le Breton N, Shi Y, Faure M, Chen Y, et al. A multidisciplinary
804 study of the emplacement mechanism of the Qingyang–Jiuhua massif in
805 Southeast China and its tectonic bearings. Part II: Amphibole geobarometry and
806 gravity modeling. *Journal of Asian Earth Sciences*. 2014;86:94-105.
807 <https://doi.org/10.1016/j.jseaes.2013.09.021>.
- 808 Wu C, Dong S, Robinson PT, Frost BR, Gao Y, Lei M, et al. Petrogenesis of high-K,
809 calc-alkaline and shoshonitic intrusive rocks in the Tongling area, Anhui Province
810 (eastern China), and their tectonic implications. *Geological Society of America*
811 *Bulletin*. 2013;126:78-102.<http://dx.doi.org/10.1130/b30613.1>.
- 812 Wu CL, Dong S, Guo HP, Guo XY, Gao QM, Liu LG, et al. Zircon SHRIMP U-Pb
813 dating of intermediate-acid intrusive rocks from Shizishan, Tongling and the deep
814 processes of magmatism. *Acta Petrologica Sinica*. 2008;24:1801-12.

- 815 Wu CL, Gao QM, Guo HP, Guo XY, Liu LG, Gao YH, et al. Petrogenesis of the
816 intermediate-acid intrusive rocks and zircon SHRIMP dating in Tongling, Anhui,
817 China. *Acta Petrologica Sinica*. 2010;26:2630-52.
- 818 Xie J, Wang Y, Li Q, Yan J, Sun W. Petrogenesis and metallogenic implications of
819 Late Mesozoic intrusive rocks in the Tongling region, eastern China: a case study
820 and perspective review. *International Geology Review*. 2018;60 (11-14):1361-80.
821 <http://dx.doi.org/10.1080/00206814.2017.1386130>.
- 822 Xie J, Yang X, Sun W, Du J. Early Cretaceous dioritic rocks in the Tongling region,
823 eastern China: Implications for the tectonic settings. *Lithos*.
824 2012;150:49-61.<http://dx.doi.org/10.1016/j.lithos.2012.05.008>.
- 825 Xie J, Yang X, Sun W, Du J, Xu W, Wu L, et al. Geochronological and geochemical
826 constraints on formation of the Tongling metal deposits, middle Yangtze
827 metallogenic belt, east - central China. *International Geology Review*.
828 2009;51:388-421.<http://dx.doi.org/10.1080/00206810802712004>.
- 829 Xu X, Lu S, Xie Q, Bai L, Chu G. SHRIMP zircon U-Pb dating for the magmatic
830 rocks in Shizishan Ore-field of Tongling, Anhui Province, and its geological
831 implications. *Acta Geologica Sinica*. 2008;82:500-9.
- 832 Xu XC, Fan ZL, He J, Liu X, Liu XY, Xie Q, et al. Metallogenic model for the
833 copper-gold-polymetallic deposits in Shizishan ore-field, Tongling, Anhui
834 Province. *Acta Petrologica Sinica*. 2014;30:1054-74.
- 835 Xu XC, Yin T, Lou JW, Lu SM, Xie Q, Chu PL. Origin of Dongguashan stratabound
836 Cu-Au skarn deposit in Tongling: Restraints of sulfur isotope. *Acta Petrologica*

- 837 Sinica. 2010;26:2739-50.
- 838 Xu, Z., Lu, X., Ling, H., Lu, J., Jiang, S., Ni, P., Huang, S., Hua, M., 2005.
839 Metallogenetic Mechanism and Timing of Late Superimposing Fluid
840 Mineralization in the Dongguashan Diplogenetic Stratified Copper Deposit,
841 Anhui Province. *Acta Geologica Sinica - English Edition*, 79(3): 405-413.
842 <https://doi.org/10.1111/j.1755-6724.2005.tb00906.x>.
- 843 Yang S-Y, Jiang S-Y, Li L, Sun Y, Sun M-Z, Bian L-Z, et al. Late Mesozoic
844 magmatism of the Jurui mineralization district in the Middle–Lower Yangtze
845 River Metallogenic Belt, Eastern China: Precise U–Pb ages and geodynamic
846 implications. *Gondwana Research*. 2011;20:831-43.
847 <https://doi.org/10.1016/j.gr.2011.03.012>.
- 848 Yang X-Y, Lee I. Review of the stable isotope geochemistry of Mesozoic igneous
849 rocks and Cu–Au deposits along the middle–lower Yangtze Metallogenic Belt,
850 China. *International Geology Review*.
851 2011;53:741-57.<http://dx.doi.org/10.1080/00206814.2010.533881>.
- 852 Zhai YS, Yao SZ, Lin XD, Zhou XN, Wan TF, Jin FQ, et al. Fe-Cu (Au) Metallogeny
853 of the Middle-Lower Changjiang Region. Geological Publishing House. 1992.
- 854 Zhang L, Zhou T, Yuan F, Fan Y, Cooke DR. Petrogenetic–metallogenetic setting and
855 temporal–spatial framework of the Yueshan district, Anhui Province, east-central
856 China. *International Geology Review*.
857 2010;53:542-61.<http://dx.doi.org/10.1080/00206814.2010.482367>.
- 858 Zhao C, Hobbs BE, Ord A. Theoretical and numerical investigation into roles of

859 geofluid flow in ore forming systems: integrated mass conservation and generic
860 model approach. *Journal of Geochemical Exploration*. 2010;106:251-60.

861 Zhao X, Coe RS. Palaeomagnetic constraints on the collision and rotation of North
862 and South China. *Nature*. 1987;327:141-4.<http://dx.doi.org/10.1038/327141a0>.

863 Zhou T, Wang S, Fan Y, Yuan F, Zhang D, White NC. A review of the intracontinental
864 porphyry deposits in the Middle-Lower Yangtze River Valley metallogenic belt,
865 Eastern China. *Ore Geology Reviews*.
866 2015;65:433-56.<http://dx.doi.org/https://doi.org/10.1016/j.oregeorev.2014.10.002>.

867 Zhou T, Yuan F, Yue S, Liu X, Zhang X, Fan Y. Geochemistry and evolution of
868 ore-forming fluids of the Yueshan Cu–Au skarn-and vein-type deposits, Anhui
869 Province, South China. *Ore Geology Reviews*. 2007;31:279-303.
870 <https://doi.org/10.1016/j.oregeorev.2005.03.016>

871 Zhou T, Yuan F, Yue S, Zhao Y. Two series of copper-gold deposits in the middle and
872 lower reaches of the Yangtze River area (MLYRA) and the hydrogen, oxygen,
873 sulfur and lead isotopes of their ore-forming hydrothermal systems. *Science in*
874 *China Series D: Earth Sciences*. 2000;43:208-18.
875 <http://dx.doi.org/10.1007/BF02911946>.

876 **Figure and Table captions**

877 **Fig. 1** (a) Tectonic sketch map of mainland China; (b) Distribution of the major
878 Cretaceous igneous rocks and related mineral deposits in the Middle-Lower
879 Yangtze Metallogenic Belt (modified from Pan and Dong, 1999; Mao et al.,
880 2011).

881 **Fig. 2** Simplified magmatism-structural map of the Tongling district, Anhui province,
882 China (The map is modified from the 1:50, 000 geological maps made by the 321
883 geological team in Anhui province, 1989).

884 **Fig. 3** Geological map of the Shizishan Orefield. The Dongguashan stock is delimited
885 by the dashed line. The age data presented in the map are collected from Wu et al.,
886 2008; Xie et al., 2009; Xu et al., 2008; Guo et al., 2013; Liu et al., 2018.

887 **Fig. 4** (a), (b) and (c) Field observations of the Dongguashan quartz diorite stock; (d)
888 and (e) Irregular intrusive contact and country rock xenoliths developed in the
889 Dongguashan stock; (f), (g) and (h) Highly deformed country rocks and its
890 deformation characters.

891 **Fig. 5** (a) Restored 3D geometry of the Dongguashan stock with locations of major
892 orebodies. (b) Stratiform orebody developed in the contact. (c) Massive
893 chalcopyrite orebody in the stock boundary. (d) vein-type orebody inside the
894 Dongguashan stock. (e) Southwest dipping syn-tectonic calcite vein in the
895 country rocks. (f) and (g) show the lower hemisphere projection
896 (Schmidt-Lambert projection) of conjugated ore veins and extensional fractures,
897 respectively.

898 **Fig. 6** (a) Cross profiles of cylinder core specimens prepared for oriented thin section.
899 (b) to (g) Photomicrographs of thin sections of the representative quartz diorite in
900 the Dongguashan stock. Abbreviations: Bt-Biotite, Hbl: Hornblende, Kfs:
901 Potassium feldspar; Mt: Magnetite; Pl-Plagioclase, Qtz: Quartz; Ser: Sericite; Sph:
902 Sphene.

903 **Fig. 7** Harker diagrams for variation of SiO₂ with other major elements from this and
904 previous studies (solid grey symbols). Samples with high and low content of SiO₂
905 are classified into Group I and Group II, respectively. Detailed data are listed in
906 supplementary Table S1.

907 **Fig. 8** Results of magnetic mineralogy analysis of representative quartz diorite
908 samples from the Dongguashan stock. (a-f) thermal magnetic curves; (h-i)
909 hysteresis loops, corrected for the paramagnetic linear trend; (k-m) isothermal
910 remnant magnetization acquisition curves and backfield applications.

911 **Fig. 9** Correlation of the magnetic parameters. a) K_m vs. P_J and b) T vs. P_J .

912 **Fig. 10** Detailed AMS results of the Dongguashan quartz diorite. The white and grey
913 stereograms are for Group I and Group II, respectively.

914 **Fig. 11** (a) Magnetic foliation of the Dongguashan stock and stereogram of foliation
915 poles, (b) Stereograms of poles of magnetic foliation for samples in Group I and
916 Group II, respectively. (c) Magnetic lineation of the Dongguashan stock with
917 inserted stereogram. (d) Stereograms of magnetic lineation for samples in Group I
918 and Group II. All the projections are equal area and lower-hemisphere.

919 **Fig. 12** (a) 3D geometric model of the Dongguashan quartz diorite stock and its
920 related ore deposits, (b), (c) and (d) Representative drilling profiles of the
921 Dongguashan, Datuanshan and Huashupo ore, respectively.

922 **Fig. 13** (a) Photograph and (b) sketch of intrusive contact in the Dongguashan stock.

923 **Fig. 14** Cartoon of the magma emplacement mechanism of the Dongguashan stock.

924

925 **Table 1** Sampling information and site-mean values of AMS results of the

926 Dongguashan quartz-diorite stock.

927

928

929 **Highlights**

930 ● The Dongguashan quartz-diorite stock was built by multiple magma pulses

931 ● Early magma pulse was guided by inherited NE-SW-trending structure in country

932 rock

933 ● Late magma pulse emplacement was assisted by regional extensional regime

934 ● Eastward magma emplace might control location of skarnization in stock eastern

935 side

936

937

Table 1. Sampling information and site-mean AMS results of the Dongguashan stock.

Site	Litho.	Depth (m)	n	Km(10^{-6} SI)	P_f	T	Site mean AMS		
							K_I	$\alpha_{95}(\text{max/min})$	D
							Dec (°)/Inc(°)	(°)	
HSP01	Qtz-diorite	-390	7	5010	1.14	0.04	250.2/70.4	15.4/4.9	
HSP02	Qtz-diorite	-390	5	17700	1.20	-0.08	111/46.3	16.5/13.2	
HSP03	Qtz-diorite	-390	5	6080	1.24	0.66	189.4/16.9	22.1/5.1	
DTS04	Qtz-diorite	-390	5	5400	1.18	0.08	141.4/82.7	17.1/10.4	
DTS05	Qtz-diorite	-390	5	662	1.02	0.03	222/56.1	22.8/11.6	
HSP06	Qtz-diorite	-460	6	1430	1.10	0.50	209.1/60.7	25/20.2	
DTS07	Qtz-diorite	-460	5	6380	1.10	-0.31	107.7/46.4	7.8/5.3	
DTS08	Qtz-diorite	-460	7	17800	1.13	0.63	267.9/36.3	19.2/6.2	
DTS09	Qtz-diorite	-460	7	11000	1.14	-0.44	186.8/81.1	16.7/8.2	
DTS10	Qtz-diorite	-460	6	977	1.03	0.02	48.5/12.4	5.4/3.9	
HSP11	Qtz-diorite	-580	5	2510	1.24	0.20	169.5/33.2	21.5/11.9	
HSP12	Qtz-diorite	-580	5	16200	1.06	0.39	227.9/23.4	11.3/7	
DTS13	Qtz-diorite	-580	5	5090	1.13	-0.07	132.4/68.4	18.2/16.9	
DTS14	Qtz-diorite	-580	5	1860	1.07	-0.14	67.9/2.1	9.6/4	
DTS15	Qtz-diorite	-580	5	2050	1.12	0.22	201.1/62.1	11.5/5.1	

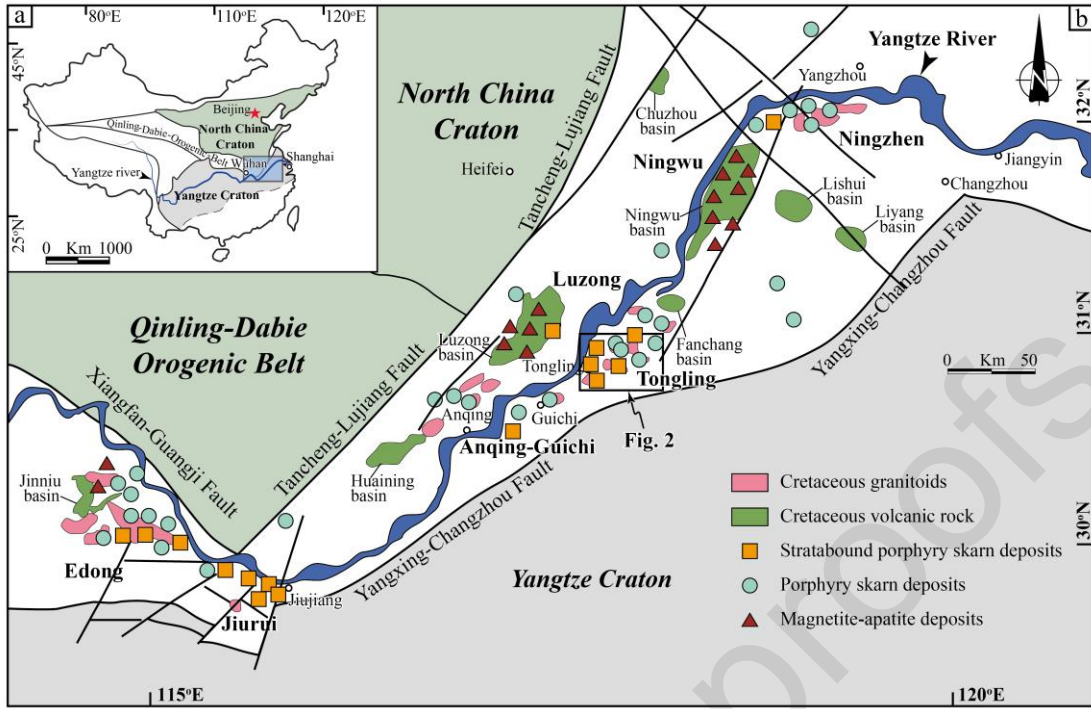
HSP16	Qtz-diorite	-670	5	8240	1.12	0.53	152.1/51.8	35.5/12.8
HSP17	Qtz-diorite	-670	5	12900	1.09	0.24	317.1/63.5	18.9/11.0
DTS18	Qtz-diorite	-670	6	4780	1.25	-0.46	137.7/72	8.1/4.1
DTS19	Qtz-diorite	-670	6	4120	1.18	0.59	135.8/17.5	51.7/13.2
DGS20	Qtz-diorite	-670	7	30200	1.08	-0.25	122.6/40.1	25.8/8.5
DGS21	Qtz-diorite	-670	6	9520	1.05	0.26	236.9/3.8	36/15.8
DGS22	Qtz-diorite	-670	5	859	1.10	0.30	260.7/37.9	38.3/13.6
DGS23	Qtz-diorite	-670	5	13900	1.10	0.08	280.5/74.3	44.6/5.1
HSP24	Qtz-diorite	-730	6	14100	1.18	-0.38	120.8/37	5.1/0.8
HSP25	Qtz-diorite	-730	5	25000	1.05	0.29	163.8/8.3	32.7/8.3
DTS26	Qtz-diorite	-730	6	16000	1.12	-0.32	319.5/19.5	7.2/3.6
DTS27	Qtz-diorite	-730	6	3380	1.12	-0.20	168.9/8.6	13.8/5.7
DGS28	Qtz-diorite	-730	6	52400	1.06	-0.02	216.4/15.3	21.7/4.1
DGS29	Qtz-diorite	-730	5	6000	1.15	0.40	263.5/27.2	63.5/5.9
DGS30	Qtz-diorite	-730	6	19900	1.06	0.11	236.1/35.8	15.3/10.7
DGS31	Qtz-diorite	-730	5	4670	1.06	0.04	300.2/10.8	5.4/4.2
HSP32	Qtz-diorite	-790	7	3650	1.22	0.21	152.6/38.2	21.3/6.4
DGS33	Qtz-diorite	-790	5	12100	1.10	0.14	224.6/65	7.8/4.5
DGS34	Qtz-diorite	-790	5	2380	1.05	-0.11	90.1/1.1	9.8/2.7
DGS35	Qtz-diorite	-790	5	39000	1.12	0.24	131/6.9	26.5/10
DGS36	Qtz-diorite	-790	7	164	1.03	0.12	275.3/2.5	15.4/5.3
HSP37	Qtz-diorite	-850	6	14400	1.19	0.14	144.9/74.1	12.1/8.9
DGS38	Qtz-diorite	-850	5	19900	1.10	-0.04	262.8/37.6	23.5/6.0
DGS39	Qtz-diorite	-850	5	41300	1.21	0.52	49.1/49.3	23.6/5.2
DGS40	Qtz-diorite	-850	5	171000	1.25	0.36	184.0/45.9	47.8/12.5
DGS41	Qtz-diorite	-850	5	33400	1.14	0.09	140.2/73.3	14.9/10.9

938 Note:

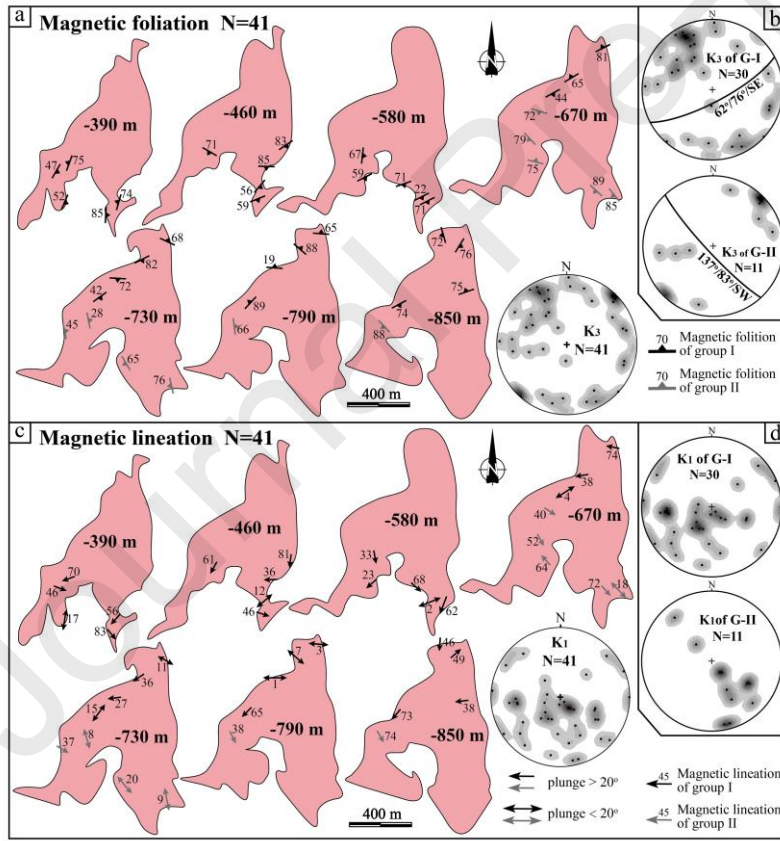
939 (1) Site: sampling site, n: number of specimen at sampling site; Km: bulk magnetic
 940 susceptibility, P₁: degree of susceptibility anisotropy, T: shape parameter of the AMS ellipsoid,
 941 K₁: Magnetic lineation, K₃: The pole of the magnetic foliation, Inc.: Inclination, Dec.:
 942 Declination, α_{95} (max/min): the long and short axes of the confidence ellipsoid at 95% level.

943 (2) The unfilled and light grey filled lines represent the data of the Group-I and Group-II sites,
 944 respectively.

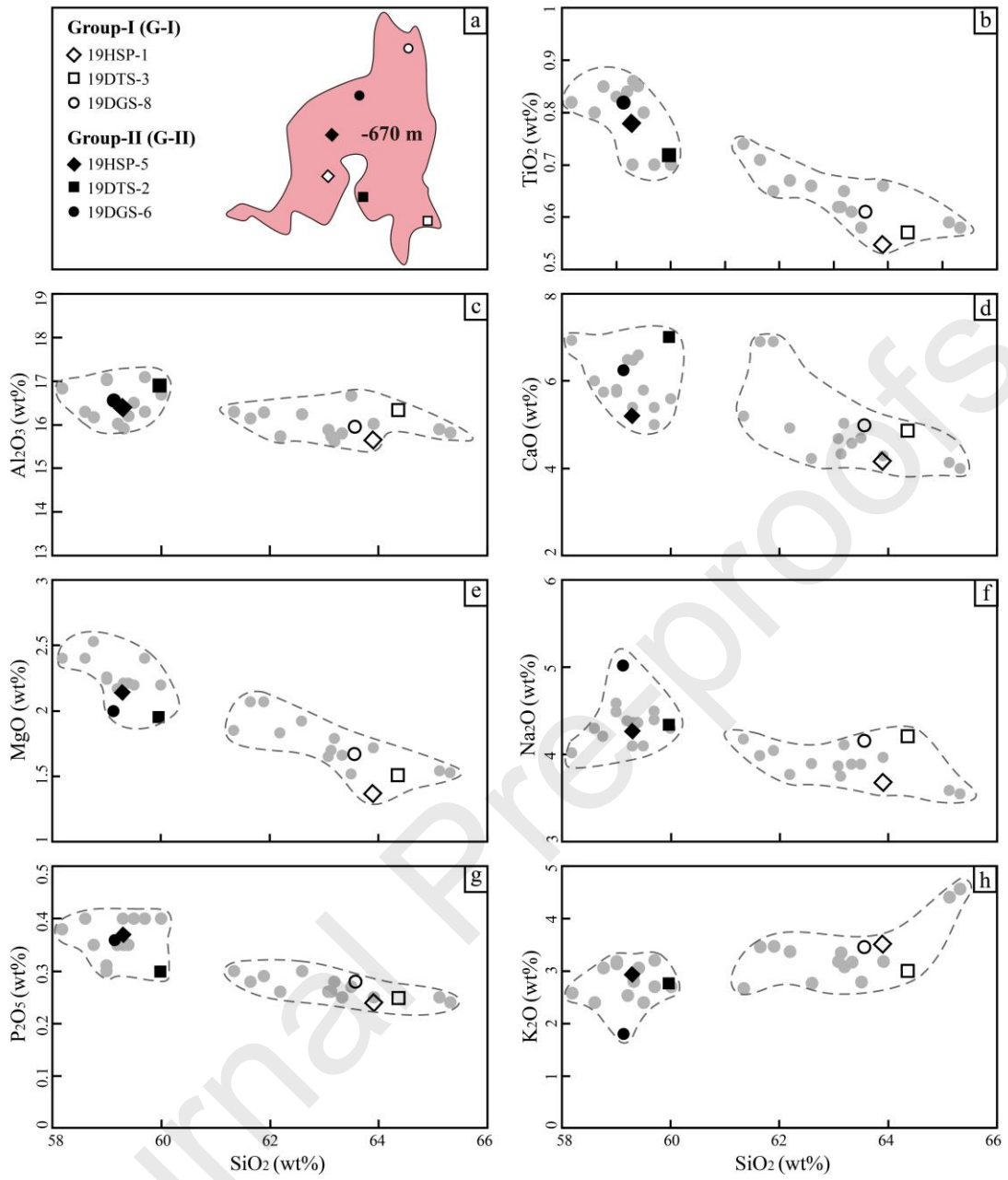
945

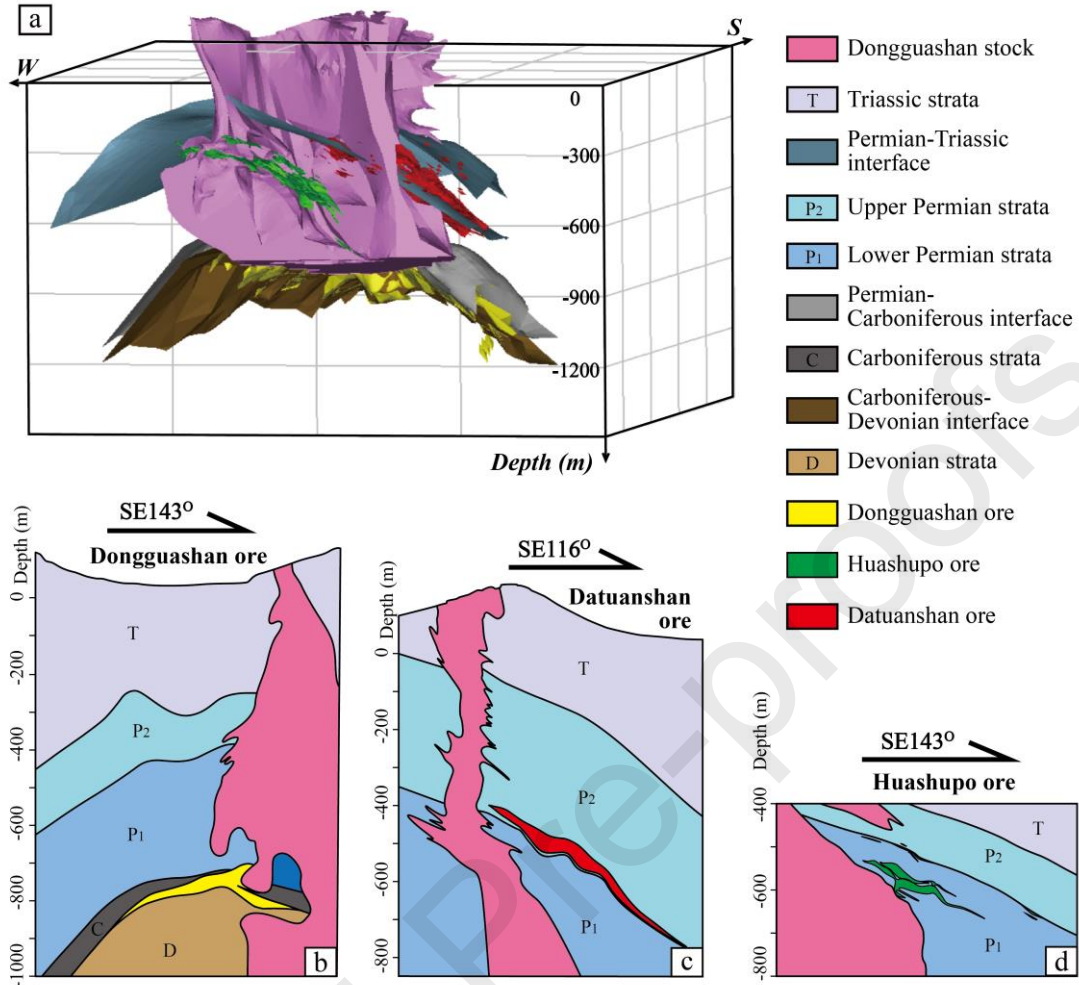


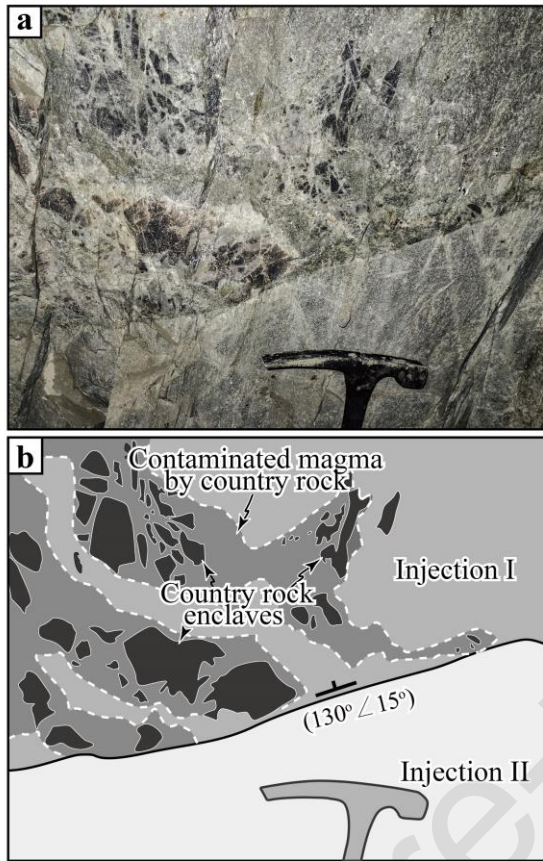
946



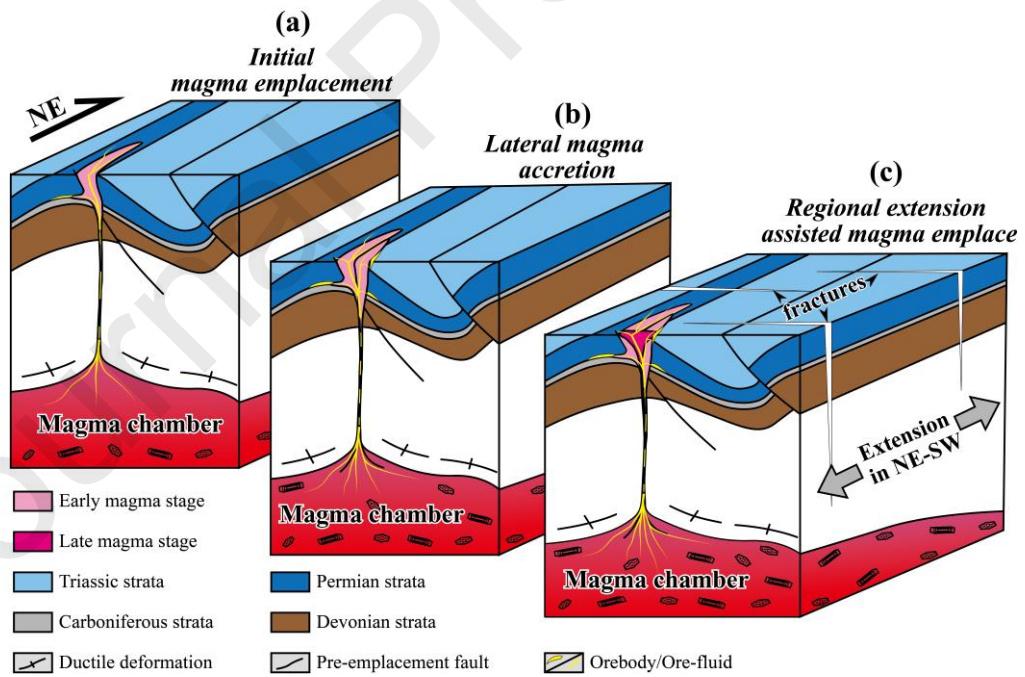
947







950



951

